

UV TO MID-IR OBSERVATIONS OF STAR-FORMING GALAXIES AT $z \sim 2$ ¹: STELLAR MASSES AND STELLAR POPULATIONS

ALICE E. SHAPLEY²

University of California, Berkeley, Department of Astronomy, 601 Campbell Hall, Berkeley, CA 94720

CHARLES C. STEIDEL, DAWN K. ERB, AND NAVEEN A. REDDY
 California Institute of Technology, MS 105-24, Pasadena, CA 91125

KURT L. ADELBERGER³

Observatories of the Carnegie Institution of Washington, 813 Santa Barbara Street, Pasadena, CA 91101

MAX PETTINI

Institute of Astronomy, Madingley Road, Cambridge CB3 0HA UK

PAULINE BARMBY AND JIASHENG HUANG

Harvard-Smithsonian Center for Astrophysics, 60 Garden Street, Cambridge, MA 02138

DRAFT: May 6, 2019

ABSTRACT

We present the broad-band UV through mid-infrared spectral energy distributions (SEDs) of a sample of 72 spectroscopically-confirmed star-forming galaxies at $z = 2.30 \pm 0.3$. Located in a 72 arcmin² field centered on the bright background QSO, HS1700+643, these galaxies were pre-selected to lie at $z \sim 2$ based solely on their rest-frame UV colors and luminosities, and should be representative of UV-selected samples at high redshift. In addition to deep ground-based photometry spanning from 0.35 – 2.15 μm , we make use of *Spitzer*/IRAC data, which probes the rest-frame near-IR at $z \sim 2$. The range of stellar populations present in the sample is investigated with simple, single-component stellar population synthesis models. The inability to constrain the form of the star-formation history limits our ability to determine the parameters of extinction, age, and star-formation rate without using external multi-wavelength information. Emphasizing stellar mass estimates, which are much less affected by these uncertainties, we find $\langle \log \frac{M_*}{M_\odot} \rangle = 10.32 \pm 0.51$ for the sample. The addition of *Spitzer*/IRAC data as a long-wavelength baseline reduces stellar mass uncertainties by a factor of 1.5 – 2 relative to estimates based on optical – K_s photometry alone. However, the total stellar mass estimated for the sample is remarkably insensitive to the inclusion of IRAC data. We find correlations between stellar mass and rest-frame R band (observed K_s) and rest-frame 1.4 μm (observed 4.5 μm) luminosities, though with significant scatter. Even at rest-frame 1.4 μm , the M/L ratio varies by a factor of 15 indicating that even the rest-frame near-IR, when taken alone, is a poor indicator of stellar mass in star-forming galaxies at $z \sim 2$. Allowing for the possibility of episodic star formation, we find that typical galaxies in our sample could contain up to three times more stellar mass in an old underlying burst than what was inferred from single-component modeling. In contrast, mass estimates for the most massive galaxies in the sample ($M_* > 10^{11} M_\odot$) are fairly insensitive to the method used to model the stellar population. Galaxies in this massive tail, which are also the oldest objects in the sample, could plausibly evolve into the passive galaxies discovered at $z \sim 1.7$ with near-IR selection techniques. In the general framework of hierarchical galaxy formation and mergers, which implies episodic star-formation histories, galaxies at high redshift may pass in and out of UV-selected and near-IR color-selected samples as they evolve from phases of active star formation to quiescence and back again.

Subject headings: cosmology: observations — galaxies: evolution — galaxies: high-redshift — galaxies: starburst — stars: formation

1. INTRODUCTION

¹ Based, in part, on data obtained at the W.M. Keck Observatory, which is operated as a scientific partnership among the California Institute of Technology, the University of California, and NASA, and was made possible by the generous financial support of the W.M. Keck Foundation.

² Miller Fellow

³ Carnegie Fellow

Within the last few years, new techniques and facilities have resulted in a burst of activity focused on understanding the progress of galaxy formation during the era near $z \simeq 2$. While this epoch has been known for some time as the peak of the “quasar era” (Schmidt et al. (1995)), until recently it has comprised part of the “redshift desert” about which little was known for normal galaxies. The recent exploration of galaxies

in the $z \sim 2$ era has occurred on a number of fronts: new surveys have now successfully identified samples of $z \sim 2$ galaxies based upon their very bright far-IR and radio emission (e.g., Chapman et al. 2004), their signature rest-frame far-UV colors (Adelberger et al. 2004b; Steidel et al. 2004), their high luminosity in the observed K band (Daddi et al. 2004b), red rest-frame optical colors (van Dokkum et al. 2003; Franx et al. 2003), or some combination of the above (e.g., Abraham et al. 2004; Shapley et al. 2004). The results of most of these surveys suggest that it was near $z \sim 2$ that galaxies as massive as any we see in the local universe began reaching maturity, and where a transition from rapidly star-forming to asymptotically quiescent may be occurring “before our eyes” for relatively massive galaxies (e.g., McCarthy et al. 2004; Daddi et al. 2004a; Shapley et al. 2004). Fortunately, galaxies in the redshift range $2 \lesssim z \lesssim 2.5$ are particularly well-suited to spectroscopic studies both in the observed optical (Steidel et al. 2004; Daddi et al. 2004b) and especially in the observed near-IR, where nebular lines valuable for measurement of kinematics, star-formation rates, and chemical abundances are observationally accessible (e.g., Erb et al. 2003, 2004, 2005; Shapley et al. 2004; van Dokkum et al. 2004).

One of the fundamental physical measurements that can be made for high redshift galaxies, and one of the more important for placing them into the theoretical context, is the stellar mass. A number of authors in the last several years have interpreted observed-frame UV to near-IR photometry with stellar population synthesis models in order to infer the stellar mass for samples of $z \gtrsim 2$ galaxies (e.g., Papovich et al. 2001; Shapley et al. 2001; Daddi et al. 2004b). Others have used similar methods and the technique of photometric redshifts to obtain measures of the total stellar mass as a function of redshift (e.g., Dickinson et al. 2003; Fontana et al. 2003; Glazebrook et al. 2004). Stellar mass measures become increasingly uncertain as one goes to higher redshift, where ground-based observations, limited to $\lambda \lesssim 2.3 \mu\text{m}$, probe increasingly shorter rest-frame wavelengths. At $z > 2$, the K_s band corresponds to the rest-frame optical, where current or recent star formation may dominate the observed luminosity rather than the stellar mass that has accumulated over a galaxy’s lifetime. For this reason, the arrival of data from the IRAC instrument (Fazio et al. 2004) on board the *Spitzer Space Telescope* (hereafter *Spitzer*) has been widely anticipated as a means to significantly improve the measurement of stellar mass and star formation history since it is capable of obtaining very sensitive observations out to $8 \mu\text{m}$, allowing photometric access to the rest-frame $1 - 2 \mu\text{m}$ light from galaxies to redshifts $z \sim 4$, and providing particularly sensitive observations of this region for galaxies with more modest redshifts near $z \sim 2$.

In this paper, we discuss the broad-band properties of a reasonably large sample of spectroscopically confirmed, UV-selected galaxies at $z \sim 2$ in a field that was observed by the IRAC “In-Orbit Checkout” (IOC) program in the early days of *Spitzer*. The principal aim has been to explore the broad-band spectral energy distributions (SEDs) for a robustly defined sample of high redshift galaxies that naturally spans a large range in stellar mass, star-formation rate, and star-formation his-

tory. The main advantages of a UV-selected sample at $z \sim 2$, described in detail elsewhere (Adelberger et al. 2004b; Steidel et al. 2004) are that confirming optical spectra can be easily obtained, photometric selection is highly efficient and requires using only relatively “inexpensive” optical ground-based photometry, and it is possible to tune color criteria to yield a roughly volume-limited sample over the desired redshift range. In this particular case, an additional advantage was that the spectroscopic sample of galaxies already existed, as did deep photometry from observed 0.35 to $2.15 \mu\text{m}$ and targeted near-IR spectroscopic observations. Details of the near-IR photometry and spectroscopy will be presented in Erb et al. (2005). The HS1700+6416 field is one of several we have used in a survey designed to combine observations of $z \sim 2$ galaxies with sensitive observations of the intergalactic medium (IGM) in the same volume. In this respect, HS1700+6416 ($z_{em} = 2.72$) is one of the very best-studied high redshift QSOs in the entire sky, due to its unusual brightness ($V \sim 16$). It also happens to lie in the “continuous viewing zone” for both *Spitzer* and HST; this fact, plus the availability of the ancillary deep ground based data, is the main reason the field was chosen for the deep IOC observations by the IRAC team.

In combination with the ground-based photometric and spectroscopic data, the IRAC observations of this field provide a means to establish the range of properties represented among galaxies selected using UV colors; these may be useful for comparison to galaxy samples at similar redshifts but selected using other techniques. Of particular interest to us is a quantitative assessment of the “value added” by longer wavelength photometry for assessing the galaxy properties at high redshifts as compared to what one would infer from ground-based measurements alone (since realistically only a fraction of ground-based fields will be observed by *Spitzer* during its lifetime). As it turns out, the HS1700 field is also interesting because it allows for a preliminary comparison of the dependence of $z \sim 2$ galaxy properties on large-scale environment (Steidel et al. 2005).

The paper is organized as follows: §2 presents the ground-based and *Spitzer* observations; §3 describes the photometry and the selection of the sample which is discussed in the rest of the paper; §4 describes the use of stellar population synthesis models to infer physical properties of the galaxies from their broad-band spectral energy distributions (SEDs); §5 summarizes the results of the modeling focusing on the galaxy stellar masses and mass-to-light ratios (M/L); §6 discusses the results and their general implications; §7 summarizes the main results.

We assume a cosmology with $\Omega_m = 0.3$, $\Omega_\Lambda = 0.7$, and $h = 0.7$ throughout.

2. OBSERVATIONS

2.1. Optical Imaging

Images of the HS1700+64 field were obtained in 2001 May using the William Herschel 4.2m telescope on La Palma and the Prime Focus Imager. The WHT system uses a 2-chip mosaic of Marconi 2k x 4k CCDs with especially good UV quantum efficiency, and provides a field of view of $16'$ by $16'$ sampled at $0''.236$ per pixel. The conditions during the observing run were excellent, with sub-arcsecond seeing in all bands. The field was roughly

centered on the position of the QSO, and 15 arcsecond dithers were executed between subsequent exposures in order to allow for fringe removal in the \mathcal{R} band and the creation of dark sky superflats (particularly necessary in the U_n band). The data were reduced using procedures described in detail by Steidel et al. (2003).

Additional images in the U_n band covering the central $5'$ by $7'$ region of the WHT field were obtained in 2001 May using the blue side of the Low Resolution Imaging Spectrometer on the Keck I 10m telescope (McCarthy et al. 1998; Steidel et al. 2004). These were scaled, variance weighted and combined with the WHT data to form the final U_n image.

Properties of the reduced and stacked images are summarized in Table 1.

2.2. Near-IR Imaging

We observed the HS1700+64 field during two observing runs, 2003 May and 2003 October, using the Palomar 5.1m Hale telescope and the Wide Field Infrared Camera (WIRC; Wilson et al. 2003). The images were taken in the K-short (K_s) filter, obtained in a sequence of 30-second integrations, moving the telescope in a prescribed dither pattern after each sequence of 4 exposures. The conditions during both observing runs were generally good, with seeing ranging between $0''.55$ and $0''.99$, but the ambient temperature was warm resulting in relatively high K_s band sky backgrounds (~ 12.4 mag arcsec $^{-2}$). The WIRC camera employs a Rockwell HgCdTe “Hawaii-2” $2k \times 2k$ array, providing a field of view of $8'.5 \times 8'.5$ with a spatial sampling of 0.249 arcsec per pixel.

The WIRC data from each (typically 54 minute) dither sequence were reduced, registered, and stacked using a set of IDL scripts written by K. Bundy (private communication). The resulting images were then registered and combined using IRAF tasks. The final K_s image represents a total of 11.03 hours of integration in the parts of the image that received the full integration time. The final mosaic was trimmed to include only the parts of the image receiving 50% or more of the total integration time ($\sim 90\%$ of the trimmed image received the full exposure time). The image was calibrated with reference to the near-IR standards of Persson et al. (1998).

2.3. Spitzer/IRAC Imaging

Observations with the Infrared Array Camera (IRAC) were obtained in 2003 October during the “In-Orbit Checkout” (IOC) of *Spitzer*. The observing strategy and data reductions are described in detail by Barmby et al. (2004). The IRAC observations were designed to overlap as much as possible with the ground-based K_s and optical images, but some compromises were adopted to avoid known foreground galaxy clusters in the field, so that the IRAC pointings were biased toward the SW relative to the ground-based data, which are centered on the bright QSO. As detailed below, the IRAC images in the 4 IRAC bands (see Table 1) completely overlap over only a relatively small fraction of the field observed in the K_s band described above, with the smallest overlap in the IRAC channel 1 ($3.6\mu\text{m}$) and channel 3 ($5.8\mu\text{m}$) images, but much larger overlap in channels 2 ($4.5\mu\text{m}$) and 4 ($8.0\mu\text{m}$). Figure 1 illustrates the regions covered

in the IRAC images compared to those covered in the Palomar K_s image.

The photometric calibrations for the IRAC images were as determined by the IRAC team (Barmby et al. 2004); however, we used a significantly different method for performing the photometry and estimating the photometric uncertainty (see 3.2), resulting in significantly more conservative (i.e. larger) estimated errors at a given flux density.

3. PHOTOMETRY

3.1. Optical and Near-IR

The observables from our ground-based images are \mathcal{R} magnitudes and isophotal $\mathcal{R} - K_s$, $G - \mathcal{R}$, and $U_n - G$ colors, with isophotes defined in the \mathcal{R} detection catalog. In order to mimic the actual observing process, we therefore estimated uncertainties in isophotal color rather than magnitude for all optical/IR bands except \mathcal{R} . The uncertainties were estimated separately for the optical and IR photometry, by adding large numbers of simulated galaxies of known magnitudes to the images and comparing their recovered photometry with their input parameters. The simulated galaxies were drawn from templates of exponential disks with scale lengths ranging from $0''.05$ to $0''.4$, smoothed to match the seeing of the individual images. For the $\mathcal{R} - K_s$ uncertainties, we selected galaxies at random within the range $21.0 < \mathcal{R} < 26.0$ and $1.0 < \mathcal{R} - K_s < 5.5$ and placed them at random positions on the \mathcal{R} and K_s images, 200 at a time (to avoid overcrowding) for a total of 250,000 fake galaxies. We then performed photometry as usual on the images, and compared the catalog of detections with the input list of simulated galaxies. We considered the quantity $\Delta[\mathcal{R} - K_s] = (\mathcal{R} - K_s)_{\text{meas}} - (\mathcal{R} - K_s)_{\text{true}}$, and binned in steps of 0.5 mag in $\mathcal{R}_{\text{meas}}$ and 0.2 mag in $(\mathcal{R} - K_s)_{\text{meas}}$. The mean value of $\Delta[\mathcal{R} - K_s]$ is an estimate of the bias in the photometry; for typical objects, $\Delta[\mathcal{R} - K_s] < 0.05$ mag. The standard deviation $\sigma(\Delta[\mathcal{R} - K_s])$ provides an estimate of the $\mathcal{R} - K_s$ uncertainty for objects that fall in each bin; this was typically $\sigma(\Delta[\mathcal{R} - K_s]) \sim 0.25$ mag. $\mathcal{R} - K_s$ uncertainties for each object are given in Table 2. Uncertainties in \mathcal{R} , $G - \mathcal{R}$ and $U_n - G$ were determined in a similar fashion, by adding large numbers of fake galaxies to the U_n , G and \mathcal{R} images and comparing their recovered and input properties, with the additional restriction that only those objects whose recovered photometry met our selection criteria were considered. We binned in \mathcal{R} and $G - \mathcal{R}$ to determine the \mathcal{R} and $G - \mathcal{R}$ uncertainties, which were typically $\sigma(\Delta\mathcal{R}) \sim 0.14$ mag and $\sigma(\Delta[G - \mathcal{R}]) \sim 0.07$ mag, and in G and $U_n - G$ to determine $U_n - G$ uncertainties, typically $\sigma(\Delta[U_n - G]) \sim 0.13$ mag. Again uncertainties for each object are given in Table 2. Similar techniques for estimating photometric uncertainties have been used in, e.g., Adelberger & Steidel (2000); Steidel et al. (2003); Shapley et al. (2001).

3.2. IRAC

We measured IRAC fluxes by first computing an empirical point spread function (PSF) for each channel by median averaging the signal from several isolated point sources located throughout the mosaiced IRAC data in the HS1700 field and normalizing the resulting PSF to

FIG. 1.— A schematic map of the survey field considered. The grayscale image is the Palomar 5m WIRC K_s image, with the positions of objects with $1.4 \leq z \leq 2.8$ marked with black circles. The colored contours (blue=IRAC/Ch 1; green=IRAC/Ch 2; yellow=IRAC/Ch 3; red=IRAC/Ch 4) indicate regions of the image that received $> 10\%$ of the total IRAC integrations time in each IRAC band, i.e., > 1.1 hours. For full resolution figure, go to <http://astron.berkeley.edu/~aes>.

have unit flux. We obtained accurate object positions ($\lesssim 0.2''$ rms uncertainty) for $>95\%$ of IRAC sources in the field from their K_s -band counterparts in the WIRC imaging of this field, or from their \mathcal{R} -band counterparts for the small fraction of objects detected in \mathcal{R} but not in K_s . We then used the empirically-determined IRAC PSF to simultaneously model the emission of all objects within a sub-image of size $24''$ surrounding each object of interest, similar to methods generally used for photometry of stellar objects in crowded fields. This procedure to some extent mitigates the effects of confusion noise, since the object positions are known *a priori* from the much higher spatial resolution K_s band image, and allows for some de-blending of objects that are only partially resolved in the IRAC images. The method is also similar to that employed by Fernández-Soto et al. (1999) and Papovich et al. (2001) for comparing ground-based near-

IR and HST/WFPC-2 photometry. Photometric errors were computed by adding in quadrature the error in the source flux (Poisson noise) and the dispersion in measured flux values found by fitting PSFs to 100 random positions containing no obvious sources near the object of interest. This latter estimate should account to a large extent for noise due to source confusion, which is particularly relevant in the 3.6 and $4.5 \mu\text{m}$ bands. Except in cases of very bright sources, the background dispersion dominates the errors. The PSF full-width at half maximum (FWHM) and approximate 5σ sensitivity limits for each channel are presented in Table 2. We omitted any measured fluxes with uncertainties larger than 0.5 magnitudes from consideration in fitting the SEDs as described in § 4.1. In addition, we set the errors to 0.10 magnitudes for measurements whose formal uncertainties calculated using the above prescription were < 0.10 magnitudes, in

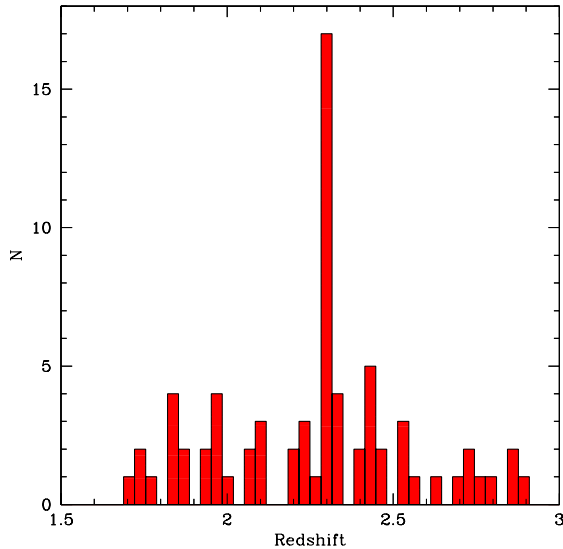


FIG. 2.— Redshift histogram for 72 spectroscopically identified galaxies in the HS1700+643 field with near-IR and IRAC detections. This histogram contains a significant spike at $z = 2.30 \pm 0.015$, discussed by Steidel et al. (2005).

order to account for systematic uncertainties in the photometry that are not otherwise accounted for (e.g., source confusion on scales smaller than the PSF, estimation of local background, etc.).

3.3. Sample Selection

Because the redshift of HS1700+643 is $z_{em} = 2.72$ and we were interested in the properties of the galaxies in the “foreground,” the spectroscopic observations targeted photometrically selected galaxies that would neatly cover the redshift range $1.9 \lesssim z \lesssim 2.7$. To accomplish this we selected a combination of objects satisfying either the “BX” photometric criteria of Adelberger et al. (2004b) ($z = 2.20 \pm 0.32$) or the “MD” photometric criteria of Steidel et al. (2003) ($z = 2.79 \pm 0.27$). A total of 100 objects (81 “BX” and 19 “MD”) has measured spectroscopic redshifts $z > 1.4$ from observations with the Low Resolution Imaging Spectrometer, described in detail in Steidel et al. (2004). Because the surface density of BX candidates is ~ 6 times higher than that of MD candidates to the same $\mathcal{R} = 25.5$ apparent magnitude limit, the expected redshift distribution for a BX/MD photometric sample, based on the total of 1133 spectroscopic redshifts for BX/MD candidates in all survey fields, is $\langle z \rangle = 2.24 \pm 0.36$.

The sample of galaxies discussed in the rest of the paper is culled from the region of overlap between the ground-based $U_n G \mathcal{R}$ images, the ground-based K_s image, the 4 IRAC bands (see figure 1) and the spectroscopic observations of UV-selected galaxies. Within the $8'.3$ by $7'.8$ region covered by the Palomar K_s image, there is a total of 508 BX and MD-type galaxy candidates identified from the optical photometry using the selection criteria defined by Adelberger et al. (2004b) and Steidel et al. (2003), respectively; of those, 389 (77%) of the objects are significantly detected in the K_s -band image. Within the 64.7 square arcmin region covered by the K_s image, we obtained spectra for 162 of the 508 photometric candidates and spectroscopically identified 98

objects. The identified fraction represents a 60.5% spectroscopic success rate, similar to that of our $z \sim 2$ survey overall (Steidel et al. 2004). As discussed in Steidel et al. (2004), we expect the unidentified objects have the same redshift distribution as the spectroscopic successes. Of the 98 objects with spectroscopic identifications, 92 are detected in the K_s image to $K_s(\text{Vega}) \sim 22$; of the 92 objects with spectroscopic IDs and K_s detections, 79 (86%) are at $z > 1.4$ and have a mean redshift and dispersion of 2.26 ± 0.30 , entirely consistent with the expected redshift distribution for all BX/MD candidates as discussed above. Of the 79 spectroscopically identified $z \sim 2$ galaxies, 72 are detected in one or more of the IRAC passbands and included in the stellar population analysis. Invariably, objects detected significantly at $2.15 \mu\text{m}$ are also detected in the IRAC 3.6 and $4.5 \mu\text{m}$ bands; the 7 galaxies detected at $2.15 \mu\text{m}$ but not with IRAC simply fall outside of the well-exposed regions of the IRAC pointings.

In summary, the 72 $z \sim 2$ galaxies discussed in this paper are representative of a UV-selected sample to $\mathcal{R} = 25.5$, but are objects which are also detected in both the near and mid-IR. The only possible bias of this sample relative to any sample selected using the same UV criteria is that it excludes the $\sim 23\%$ of BX/MD candidates in the field that are not detected to $K_s \sim 22$. The redshift distribution for this spectroscopic sample with near and mid-IR detections is shown in figure 2. Very strikingly, there is a significant galaxy overdensity in this distribution at $z = 2.30$, which allows for an examination of galaxy properties as a function of large-scale environment (Steidel et al. 2005).

It is of interest, for some purposes, to ask what fraction of a mid-IR selected galaxy sample at the same redshift is represented by objects selected using the UV color criteria. This is a difficult question to answer, as there is as yet no large spectroscopic sample of mid-IR selected high redshift galaxies (and, as we argue below, photometric redshifts may be an inadequate approach to the problem). However, we can make a rough estimate as follows. Recently, Barmby et al. (2004) suggested a region in IRAC 3.6/4.5/5.8 μm color space that may make it possible to select high redshift galaxies from IRAC colors alone, based on models and the observed locations of $z \sim 3$ UV-selected galaxies in IRAC color space. In figure 3 we show the locations in the $U_n G \mathcal{R}$ color plane of all of the objects detected in the K_s band that are within the region of the IRAC images covered by IRAC at 3.6, 4.5, and $5.8 \mu\text{m}$ and which have IRAC uncertainties of < 0.3 mag in each band.⁴ Out of a total of 618 galaxies with K_s , $3.6 \mu\text{m}$, $4.5 \mu\text{m}$, and $5.8 \mu\text{m}$ measurements, 443 are included in the optical photometric catalog to $\mathcal{R} = 25.5$, 99 of which satisfy the criteria proposed by Barmby et al. (2004) in the 3.6-5.8 μm color space. As shown in figure 3, 46 of the 99 sources satisfying the Barmby et al. color criteria do indeed lie in the regions of $U_n G \mathcal{R}$ color space from which $z \sim 2$ BM ($z = 1.70 \pm 0.34$), BX ($z = 2.20 \pm 0.32$), MD ($z = 2.72 \pm 0.3$) and C/D/M ($z = 3.0 \pm 0.3$) (Steidel et al. 2003) galaxies are drawn.

⁴ The size of this region is approximately 30 arcmin^2 , although only $\sim 40\%$ of the objects in a K_s -selected catalog within this region are included, primarily because of the limited depth of the $5.8 \mu\text{m}$ image.

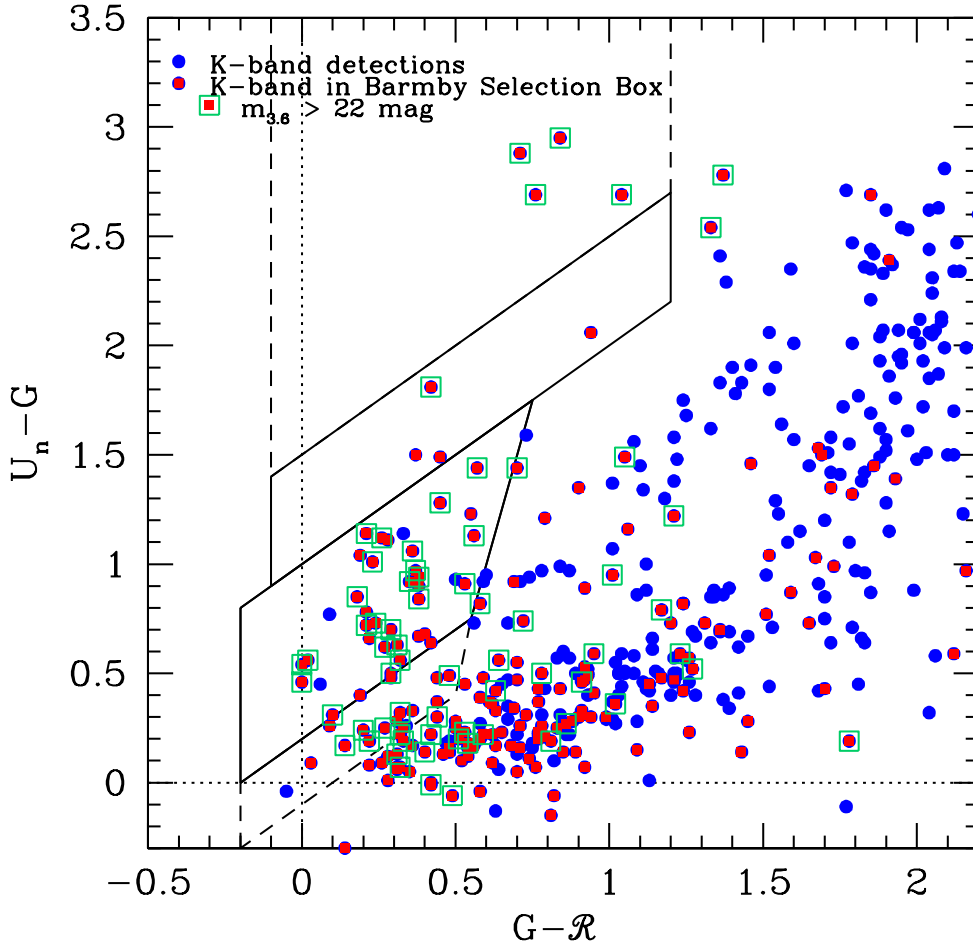


FIG. 3.— Plot showing the location in optical U_nGR color space of all objects in a K-selected catalog to $K \simeq 22$. The regions within the solid black lines denote those used to select the galaxies discussed in this paper (“BX” and “MD”); the dotted curves denote regions containing “BM” ($z = 1.7 \pm 0.3$, lower left) and “C/D” LBGs ($z = 3.0 \pm 0.3$, upper left). Objects satisfying the “high z ” galaxy criteria suggested by Barmby et al. (2004) based on IRAC colors are marked in red. As discussed in the text, a significant fraction ($\sim 40\%$) of the IRAC “high z ” objects in the optical catalog appear to lie at $z < 1.4$.

However, there is a significant number of galaxies (~ 40) which satisfy the Barmby et al. criteria but are located in regions inhabited primarily by $z \sim 0.7 - 1.5$ star forming or passive galaxies in optical color space (see, e.g., Adelberger et al. 2004b). Another ~ 10 have optical colors that are outside of the UV selection windows, but are consistent with more reddened star forming galaxies at $z \sim 1.5 - 2.5$ (cf. Daddi et al. 2004a). Of the 175 galaxies that are well detected in the K_s , 3.6, 4.5, and 5.8 μm bands but absent from the optical catalog, 81 satisfy the Barmby et al. color criteria. Assuming that the same percentage ($\sim 40\%$) of these are likely to be in the foreground as for the optically detected galaxies, ~ 50 galaxies to $K_s \sim 22$ are plausibly at $z \gtrsim 1.5$ ⁵. Most of

the galaxies in this red sample are relatively faint in the K_s band, with only 12 of 81 having $K_s < 20$, of which perhaps 6-8 are high redshift objects.

In summary, of the 180 galaxies well detected in the K_s , 3.6, 4.5, and 5.8 μm bands that also satisfy the Barmby et al. criteria, 46 would be selected based on U_nGR colors to be at $z \gtrsim 1.5$, ~ 70 ($\sim 40\%$) are likely to be at $z \lesssim 1.5$, while the remaining ~ 60 galaxies are plausible $z \gtrsim 1.5$ candidates that do not satisfy the U_nGR selection criteria. Thus, we conclude that $\sim 50\%$ of galaxies at $z \sim 2.3 \pm 0.4$ to an apparent magnitude limit of $K \sim 22$ ($K \sim 23.8$ on the AB system) would be selected using the rest-UV color criteria to $\mathcal{R} = 25.5$. This statistic is broadly consistent with the results of the FIRES survey (Franx et al. 2003) which targeted galaxy-

⁵ 29 of the 81 objects are actually detected in the \mathcal{R} band to $\mathcal{R} \sim 26$ but are not included in figure 3 because the colors are not

reliably measured.

ies with colors $J - K > 2.3$, most of which are similarly optically faint, as well as with the “IRAC EROs” discussed by Yan et al. (2004). We defer further discussion of the overlap and distinctiveness of samples selected in various ways to future work.

4. POPULATION SYNTHESIS MODELING

4.1. Sample

In order to explore the stellar populations of UV-selected $z \sim 2$ galaxies in the HS1700+64 IRAC pointing, we considered only the subsample of 72 galaxies with measured redshifts, K_s magnitudes, and IRAC detections in at least one channel. As discussed below, the set of colors and magnitudes for BX and MD galaxies is not sufficient to simultaneously determine accurate photometric redshifts and stellar masses for galaxies that do not have spectroscopic redshifts.

The photometric measurements used to model the stellar populations are given in Table 2. Note that all of the magnitudes and colors are on the AB system, with the exception of the $\mathcal{R} - K_s$ color, for which the K_s mag is on the Vega system for easier comparison to other work on similar high redshift galaxies.⁶ For the 13 galaxies at $z > 2.5$, we did not include the $U_n - G$ color in the SED fit, since absorption by H I in the intergalactic medium begins to have a strong effect on the measured U_n magnitude at these redshifts.

Before modeling the galaxy magnitudes and colors, we corrected the U_n or G magnitude for the effects of galactic Ly α emission and absorption. Ly α equivalent widths were measured from the LRIS spectra used to identify redshifts. These corrections were applied to galaxies at $z = 1.7 - 1.9$ (U_n) or $z > 2.47$ (G). We also have H α and [NII] emission line measurements for four galaxies in the HS1700 sample (BX691, BX717, MD103, and MD109, all from Erb et al. (2003)). We corrected the observed K_s by 0.10, 0.17, 0.08, and 0.10 magnitudes, respectively to account for the contribution of nebular emission to the observed flux. K_s magnitudes for the remainder of the galaxies in the redshift range $2.016 < z < 2.504$ remain uncorrected. Based on a much larger sample of H α spectra of galaxies in the same redshift range (which will be discussed in detail by Erb et al. (2005)), the typical correction to the broad-band K_s flux is $+0.09 \pm 0.07$ magnitudes, although some of the most extreme cases have H α equivalent widths large enough to change the K_s magnitude by as much as several tenths of a mag. The possible impact of the K_s corrections on the modeling results is discussed below.

Only 22% of the BX/MD photometric candidates with both K_s photometry and measurements in at least one IRAC band are spectroscopically identified, and we restrict the stellar population modeling to this spectroscopic sample. To test the potential success of modeling photometric candidates without redshifts, we tried to fit simultaneously the redshift and stellar population parameters for the sample of galaxies with spectroscopic redshifts, pretending that the redshift was an undetermined free parameter. With only U_nGRK_s plus IRAC photometry, we obtained an accuracy of $\langle |z_{phot} - z_{spec}| / (1 + z_{spec}) \rangle = 0.09$. At the mean red-

shift of the sample, this error corresponds to a typical $|z_{phot} - z_{spec}|$ of 0.3, while in several cases the redshift estimates fail catastrophically, with $|z_{phot} - z_{spec}| > 1$. We note that this accuracy is very similar to that found for photometric redshift estimates in the FIRES survey, based on 39 galaxies with spectroscopic redshifts in the *Hubble Deep Field South* (HDF-S) (Rudnick et al. 2003; Labbé et al. 2003). Perhaps more significantly, the stellar population parameters inferred when simultaneously fitting for the redshift do not uniformly agree with those found when the redshift is known. Specifically, we find a typical fractional stellar mass difference of $\langle |M_*^{phot} - M_*^{spec}| / M_*^{spec} \rangle = 0.56 \pm 1.23$, which is larger than any of the fractional stellar mass uncertainties we find due to photometric uncertainties, or uncertainties in our choice of star-formation history for single-component models (see discussion in section 5.2). Not only is the scatter in this fractional offset quite large, but the distribution is skewed toward overestimating the mass, such that the average $\langle (M_*^{phot} - M_*^{spec}) / M_*^{spec} \rangle = 0.37 \pm 1.30$.⁷ This exercise demonstrates that, with only U_nGRK_s plus IRAC photometry, even for objects known to have redshifts in the targeted range (which presumably reduces the probability of catastrophic failures), considerable uncertainties would be introduced if objects without spectroscopic redshifts were included.

4.2. Modeling Procedure

Following a procedure similar to that of Shapley et al. (2001) and Shapley et al. (2004), we apply Bruzual & Charlot (2003) models to fit the SEDs of the UV-selected $z \sim 2$ galaxies in the HS1700 *Spitzer* pointing. We used models with solar metallicity and a Salpeter initial mass function (IMF) extending from $0.1 - 100 M_\odot$. Also, as recommended by Bruzual & Charlot (2003), we adopted the Padova 1994 stellar evolution tracks. Papovich et al. (2001) have investigated how the best-fit parameters depend systematically on the choice of metallicity and IMF, though we will not include such a discussion here. We do note that, at least for galaxies bright in the rest-frame optical ($K_s \leq 20$), solar metallicity appears to be a good approximation, and typical $z \sim 2$ galaxies appear to have metallicities that are only slightly lower than solar (Shapley et al. 2004). We also note that it is well established that a Salpeter IMF over-predicts the number of stars less massive than $1 M_\odot$ (or, alternatively, that it over-predicts the stellar M/L) compared to observations in the local universe (e.g., Bell et al. 2003). We use the Salpeter IMF to facilitate comparison with other work (e.g., Cole et al. 2001; Shapley et al. 2001); use of the Chabrier (2003) IMF, the IMF proposed by Baldry & Glazebrook (2003), or the “diet” Salpeter IMF used by Bell et al. (2003), would reduce the inferred stellar masses by a factor of $\sim 1.5 - 1.8$. Dust extinction is taken into account with a Calzetti et al. (2000) starburst attenuation law. Reddy & Steidel (2004) have shown that using the Calzetti law and continuous star-formation models to infer unobscured star-formation

⁶ K_s magnitudes or $\mathcal{R} - K_s$ colors may be converted to the AB system by adding 1.82 to the tabulated values.

⁷ When we exclude five galaxies with wildly discrepant M_*^{phot} relative to M_*^{spec} (all are overestimates), we find a relatively symmetric distribution around zero, with $\langle (M_*^{phot} - M_*^{spec}) / M_*^{spec} \rangle = 0.07 \pm 0.44$.

rates from UV colors and magnitudes accurately predicts the *average* X-ray and radio continuum fluxes of $z \sim 2$ star-forming galaxies, though the object to object scatter may be large. In order to determine how well the stellar population parameters can be constrained, we investigated a range of star-formation histories of the form $SFR(t) \propto \exp(-t/\tau)$, with e-folding times of $\tau = 0.01, 0.05, 0.10, 0.2, 0.5, 1, 2$, and 5 Gyr, as well as continuous star-formation (CSF) models. For the main analysis, we did not consider more complex star-formation histories, such as short-duration bursts occurring at random past times superimposed on a smoothly declining star-formation history. The data for most galaxies do not place strong constraints among the range of simple, single-component star-formation histories considered, and therefore the use of a more complex model does not seem justified. We only briefly employ extreme two-component models in section 5.4, in order to determine how much stellar mass could be contained in these galaxies in maximally old underlying bursts.

Our goal was to constrain the stellar population parameters of each galaxy. The fitted parameters included: dust extinction (parameterized by $E(B - V)$), age (t_{sf}), star-formation rate (SFR), stellar mass (M_*), and star-formation history (τ). For each τ , we used a grid of Bruzual & Charlot (2003) models with ages ranging between 1 Myr and the age of the Universe at the redshift of the galaxy being modeled and extinctions ranging between $E(B - V) = 0.0$ and $E(B - V) = 0.7$ (though none of the galaxies has a best-fit $E(B - V) > 0.5$). For each combination of $E(B - V)$, t_{sf} , and τ , we computed the full U_nGRK_s plus IRAC 3.6 – 8.0 μm SED of the model placed at the redshift of the observed galaxy. In computing this SED, we reddened the intrinsic model galaxy spectrum by dust, and further attenuated it in a manner simulating absorption by the intergalactic medium of neutral hydrogen (Madau 1995), which affects the predicted U_n and G magnitudes. Bruzual & Charlot (2003) CSF models are by default normalized to have star-formation rates of $1 M_\odot \text{yr}^{-1}$, while declining models are normalized to have a total mass of $1 M_\odot$ at $t = \infty$. We searched for the model normalization that minimized the value of χ^2 with respect to the measured SED, which yielded an estimate of the star-formation rate and stellar mass. The combination of $E(B - V)$, t_{sf} , τ and normalization yielding the lowest χ^2 was called the overall “best-fit”. Figure 5 shows the overall best-fit model together with the observed data points for each of the 72 galaxies in the sample. In most cases the “best-fit” τ model is not significantly better than that of the best-fitting model for every other value of τ considered, as discussed below.

4.3. Systematic Uncertainties

Even neglecting the effects of photometric uncertainties, parameters derived from SED fitting are subject to significant degeneracies and systematics, primarily because of the inability to constrain the star-formation history (Shapley et al. 2001; Papovich et al. 2001). These uncertainties apply even using the simplest single-component models, as we do here, since the best-fit age, extinction, and star-formation rate all depend systematically on the τ used to describe the star-formation

history. Stellar mass estimates are more robust in the face of uncertainties in the star-formation history. Here we review the systematic uncertainties in age, extinction, star-formation rate, and stellar mass that result from population synthesis modeling of galaxy SEDs at high redshift.

The inferred age, t_{sf} , for a given value of τ is constrained mainly by the magnitude of the age-sensitive Balmer break. A given Balmer break strength indicates the relative number of A and O stars and corresponds to older ages when larger values are assumed for τ (i.e. a given relative number of A/O stars is reached at later times for more gradually declining star-formation histories).

The inferred extinction, $E(B - V)$, also depends systematically on the star-formation history: declining star-formation histories with $t_{sf}/\tau > 1$ with less dust extinction can produce similar $G - \mathcal{R}$ and $\mathcal{R} - K_s$ colors to those of a model with a larger τ , smaller t_{sf}/τ and more dust extinction. In this case, the reddening of the rest-frame UV slope is caused by a mixture of stars with later spectral types on average for models with smaller τ , whereas dust extinction accounts for the UV reddening in continuous star-formation models or those with larger values of τ .

The systematic dependence of the inferred SFR on the value of τ that parameterizes the star-formation history stems from two effects. First, the star-formation rate is derived from the extinction-corrected UV-luminosity. It therefore depends on the best-fit value of $E(B - V)$, which as we discussed above, depends on the star-formation history used to model the observed SED. Second, a conversion from extinction-corrected UV-luminosity to SFR is required. This conversion depends on both t_{sf} and τ , and for a given galaxy, is generally an increasing function of τ . The conversion from UV-luminosity to SFR equilibrates after about 100 Myr for models with $\tau \geq 1$ Gyr (Kennicutt 1998). However, the ratio of SFR to UV luminosity declines as a function of time for models with smaller τ . In the range of parameter space spanned by the galaxies in our sample, $\tau = 100$ Myr models typically have UV-to-SFR conversions 1.2 – 1.8 times lower than continuous SFR models that fit the same colors. While not likely, based on external (spectroscopic) information, models with $\tau = 10$ Myr have much more extreme conversions from UV-luminosity to SFR, as much as 25 – 1000 times lower than the limit approached by the models with large τ . This is easily understood since the largest $\tau = 10$ Myr age that can reasonably fit the observed colors of the galaxies in our sample is roughly $t_{sf} \sim 100$ Myr. At this point, the star-formation rate is roughly 20000 times lower than at $t_{sf} = 0$. However, the UV-luminosity has only declined by a factor of ~ 20 , because while there are no O-stars left, the lifetime of late B-stars is roughly 100 Myr, so they have not yet disappeared.

Our single-component-model estimates of stellar masses are not plagued by the same amount of systematic uncertainty, especially when considering more realistic exponential timescales, $\tau \geq 100$ Myr. There has been much discussion in the literature about the value of rest-frame near-IR photometry in measuring stellar masses (Glazebrook et al. 2004; Bell et al. 2003). In fact, as shown by the model fits to BX490 and BX505,

FIG. 4.— Examples of confidence intervals obtained from Monte Carlo modeling for three different galaxies selected to span a range of inferred properties, as described in the text (BX879, BX691, and BX563). The confidence intervals have been projected onto the spaces of (E(B-V),Age) and (Age,Mass), and the dark and light contours correspond to 68% and 95% confidence ranges, respectively. While the time constant, τ , is treated as a free parameter ranging from 10 Myr to ∞ , the grid in τ contains only ten distinct values. The discrete nature of τ translates into discrete regions of parameter space, that would be connected smoothly if τ were allowed to vary continuously. This effect is conveyed most clearly in the (E(B-V),Age) plots, since both parameters systematically depend on τ . For full resolution figure, go to <http://astron.berkeley.edu/~aes>.

which have very similar rest-frame near-IR magnitudes, rest-frame near-IR photometry alone is insufficient to constrain the stellar mass-to-light ratio of star-forming galaxies to better than a factor of 10 (see also §5.4). However, with rest-frame UV, optical, and near-IR photometry, the near-IR M/L ratio (and therefore the stellar mass) is reasonably well-determined, almost independent of the value of τ used to fit the SED. With measurements of the rest-frame UV slope (observed $G - \mathcal{R}$ color at high redshift), the rest-frame UV/optical color (observed $\mathcal{R} - K_s$), and rest-frame UV/near-IR color (observed $\mathcal{R} - \text{IRAC}$), the variance in inferred near-IR M/L ratio due to uncertainties in the form of the star-formation history (for $\tau \geq 100$ Myr) is typically 10%. The relationship between ($G - \mathcal{R}$, $\mathcal{R} - K_s$, $\mathcal{R} - \text{IRAC}$) and M/L ratio starts to break down for star-formation histories with $\tau < 100$ Myr. The systematic uncertainty in the M/L ratio therefore increases, except in the cases where $t_{sf} \leq 10$ Myr (and $\leq \tau$ for all star-formation histo-

ries under consideration), when all star-formation histories yield the same best-fit stellar population parameters. However, for most galaxies in the sample, there is no indication that models with $\tau \leq 100$ Myr with $t_{sf}/\tau > 1$ are preferred, and in some cases such star-formation histories are actually ruled out (see discussion in section 6.2).

External constraints can be used to evaluate the likelihood that these extreme “decaying burst” star-formation histories are realistic. For example, Reddy & Steidel (2004) have shown that the mean extinction-corrected star-formation rate for $z \sim 2$ galaxies in the Chandra Deep Field North, inferred from rest-frame UV luminosities and colors, assuming > 100 Myr of continuous star formation and the Calzetti extinction law, agrees very well with the average star-formation rate derived from stacked X-ray and radio images of the same galaxies. If $\tau < 100$ had been assumed, the average UV-derived star-formation rate would have been several times smaller, and no longer in agreement with the star-formation rate

inferred from the average X-ray or radio continuum flux. In principle, the degeneracies that affect primarily the interpretation of the UV continuum slope can be removed if there is external information on the number of massive stars still present in the galaxies. For example, using observed $H\alpha$ fluxes and/or high quality far-UV spectra, it is relatively easy to establish whether O stars are still present in the galaxy spectra. In general, the high success rate in detecting $H\alpha$ emission from UV-selected galaxies, and in particular the fact that the star-formation rate inferred from $H\alpha$ fluxes is never smaller than that inferred from the UV continuum (e.g., Erb et al. 2003), suggests that it must be quite rare to catch a starburst with $t_{SF}/\tau \gg 1$ and $\tau \leq 100$ Myr. Additionally, in the individual LRIS rest-frame UV spectra with sufficient S/N, one sees evidence for the existence of massive stars from the presence of C IV and Si IV P-Cygni stellar wind features, and, in some cases $Ly\alpha$ emission. If $\tau < 100$ Myr and t_{sf}/τ were much greater than 1 in most cases, we would not expect to find such strong evidence for massive O stars in the rest-frame UV spectra of these objects.

The systematic effects discussed above do not include the uncertainties that result from including models with underlying short bursts of different strengths occurring at random times in the past (Kauffmann et al. 2003). We did not add that layer of complexity to our modeling procedure, given the difficulty we found in distinguishing among even simple exponentially declining and continuous star-formation histories. However, as Papovich et al. (2001) demonstrated, underlying maximally old bursts with $t_{sf} \gg \tau$ can increase the M/L by a factor of a several without having an appreciable effect on the rest-frame UV-to-optical colors. Glazebrook et al. (2004) find that including random bursts into the range of star-formation histories used to fit the $VIz'K$ colors of $1.0 \leq z < 2.0$ galaxies causes the derived masses to increase by less than a factor of two, although the amount by which one might be underestimating the true stellar mass will depend on the observed galaxy colors. We return to this question in section 5.4.

4.4. Monte Carlo Confidence Intervals based on Photometric Errors

In addition to the best-fit stellar population parameters for each galaxy, we also found the parameter confidence intervals allowed by the photometric uncertainties. A large set ($n = 1000$) of fake SEDs was generated for each galaxy, by perturbing the observed SED in a manner consistent with the estimated photometric error bars (sections 3.1 and 3.2). Each perturbed SED was fit in exactly the same manner as the observed SED, and a set of best-fit stellar population parameters was chosen to minimize χ^2 with respect to the perturbed SED.

We determined the confidence intervals over $E(B-V)$, t_{sf} , SFR, M_* , and τ , such that 68.3% and 95.4% confidence intervals contain the corresponding fractions of the Monte Carlo realizations. More than half of the galaxies in our sample have 95.4% confidence intervals that span all τ values, indicating the difficulty of distinguishing among the different star-formation histories with broad-band photometry alone. In practice, the most useful number we derive from the Monte Carlo confidence intervals for each galaxy is the uncertainty on the stellar mass. For this quantity, it is important to know not only the random effects of photometric errors, but also the systematic effect of allowing τ to vary. The 1σ Monte Carlo stellar mass uncertainties in column 7 of Table 3, derived from simulations in which τ was allowed to vary, reflect the uncertainty in τ . We also list the Monte Carlo stellar mass uncertainties for CSF star-formation histories in Table 3.

To demonstrate the covariance of different parameters, and at least some of the range of stellar populations present in our sample, we show in figure 4 the t_{sf} vs. $E(B-V)$ and M_* vs. t_{sf} confidence intervals derived from Monte Carlo simulations. These confidence intervals do not assume a fixed value for τ , but are the results of simulations in which τ was allowed to vary. The confidence intervals displayed include those of BX879 ($z = 2.308$), which appears to be a very young ($t_{sf} \leq 10$ Myr), dusty stellar population with high instantaneous star-formation rate and low stellar mass, all of which parameters are independent of τ because of the extremely young age; BX691 ($z = 2.190$), an evolved stellar population with $t_{sf}/\tau > 1$, τ constrained to be between 0.5 and 2 Gyr, moderate current star-formation rate and large stellar mass; and BX563 ($z = 2.296$), for which there are no constraints on the star-formation history, but the stellar mass of which is close to the sample median. The large extent of the BX563 confidence interval in t_{sf} vs. $E(B-V)$ space demonstrates some of the fundamental limitations of population synthesis modeling.

4.5. Caveats to the Model Results

The goal of population synthesis modeling is to infer physical quantities from observed galaxy magnitudes and colors, in particular the stellar mass. In the best-case scenario we would also like to place constraints on the timescale of the current star-formation episode, and therefore the level of dust extinction and the dust-corrected star-formation rate. There are certain limitations of the modeling procedure, however, that are worth pointing out, in addition to the systematic uncertainties

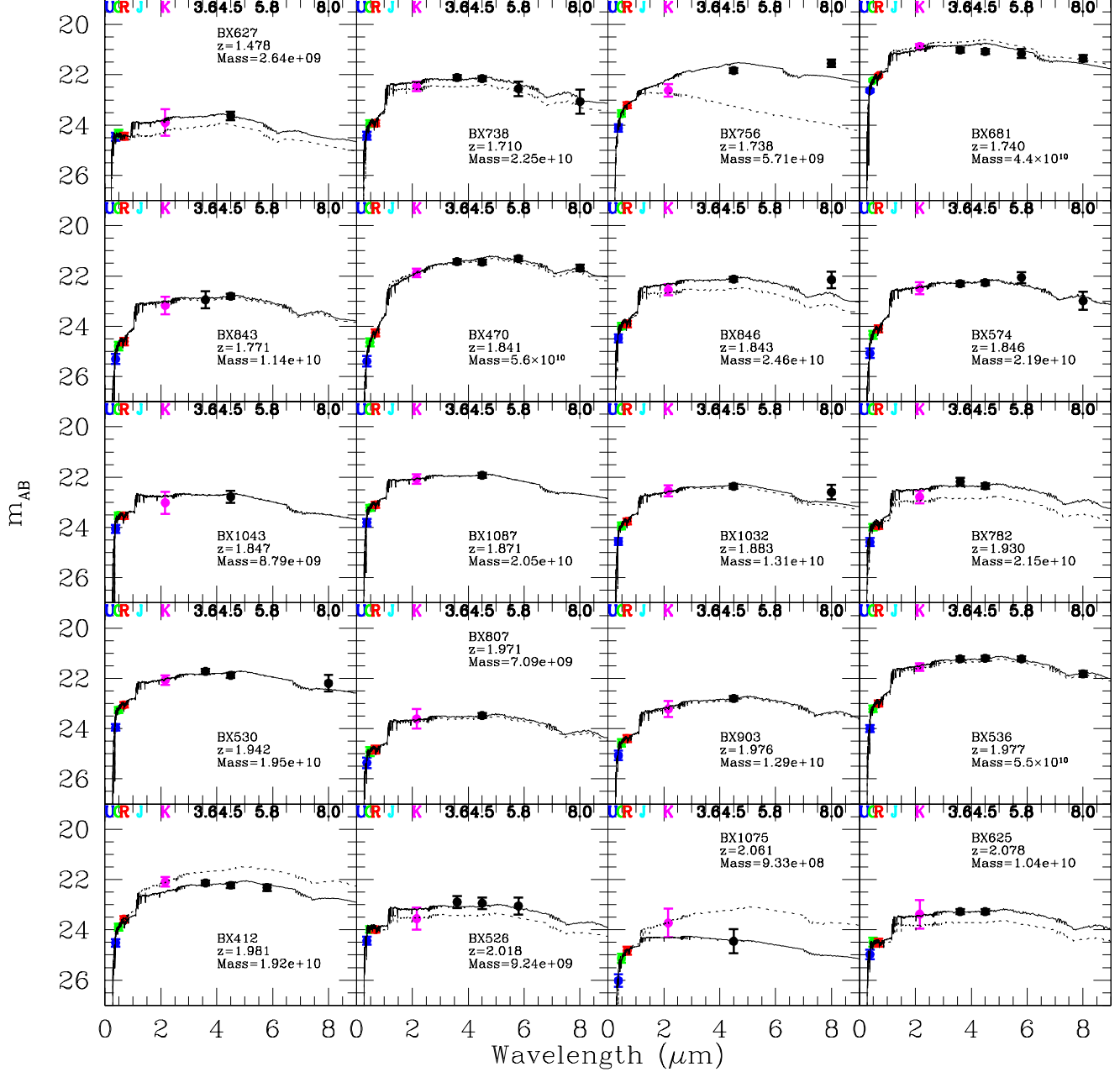


FIG. 5.— Observed and model SEDs for all 72 of the galaxies with spectroscopic redshifts and measurements in the K_s band and at least one IRAC channel, sorted by redshift from lowest to highest. The numbers for the inferred stellar mass are taken from the best-fitting exponentially declining model, which is shown with a solid curve. The dotted curve represents the best-fit model when the IRAC data points are excluded.

discussed in section 4.3.

First, it is not always possible to find a statistically acceptable fit to the observed galaxy colors, especially using relatively simple models. Seven galaxies in the sample have best-fit models with significantly higher χ^2 values than those of the rest of the sample. Two of these galaxies (BX490 ($z = 2.403$) and BX794 ($z = 2.253$)) have large $\mathcal{R} - K_s$ residuals that are likely to be explained in terms of contamination from $H\alpha$ emission in the K_s band. Another galaxy, BX561 ($z = 2.426$), has a good fit except for the IRAC $8.0 \mu\text{m}$ point, which yields a significant positive residual, possibly due to the presence of

an obscured AGN (see §5.5). MD157 shows rest-frame UV spectroscopic evidence for hosting a broad-line AGN, which probably contaminates the K_s flux (strong $H\alpha$) and IRAC $8.0 \mu\text{m}$ band. The SEDs of the remaining three galaxies (BX581 ($z = 2.406$), BX756 ($z = 1.738$), and BX681 ($z = 1.740$)) are very difficult to understand, with both large K_s and IRAC residuals that are both positive and negative, and don't stem from obvious irregularities in any of the imaging data.

A second issue is the apparent discrepancy between model parameters based on the best fit to broad-band photometry and those inferred from rest-frame UV spec-

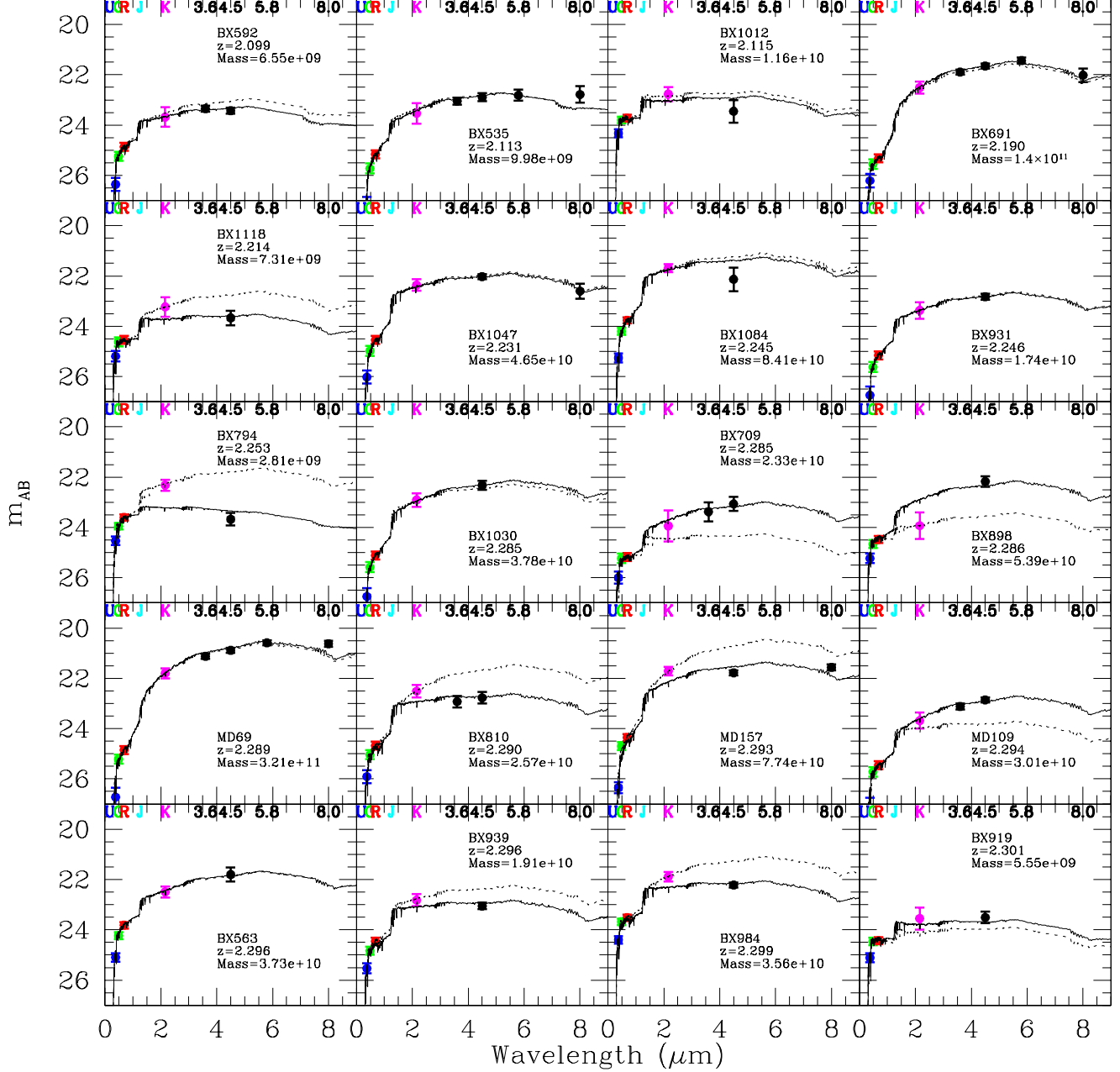


FIG. 5.— (continued)

tra, which applies for a small number of galaxies in the sample: BX1032 ($z = 1.883$), BX1087 ($z = 1.871$), and BX536 ($z = 1.977$). Not only did we obtain statistically acceptable fits to the observed photometry of these galaxies, but also the results of the Monte Carlo simulations appear to rule out star-formation histories with $\tau > 200$ Myr, and to favor best-fit t_{sf}/τ significantly greater than unity, with quite modest star-formation rates of a few $M_{\odot}\text{yr}^{-1}$. The broad-band photometry of these galaxies implies star-formation histories in which the bulk of stellar mass formed in the past, and the current star-formation rate is much lower than the past average. We also have rest-frame UV Keck I/LRIS spectra for these galaxies, which can be used as a consistency

check on the stellar population parameters derived from the SED-fitting procedure. The spectra of BX1032 and BX1087 both show prominent C IV P-Cygni features, which are produced in the winds of massive stars, associated with active ongoing star formation. The rest-frame UV spectra of BX1087 and BX536 both contain broad He II emission, which is produced by Wolf-Rayet stars, another indication of a young stellar population. Finally, the spectrum of BX1032 exhibits nebular emission lines such as CIII] and He II, further indications of active current star formation. In short, the rest-frame UV spectra of these $t_{sf}/\tau \gg 1$ galaxies contain features that are not consistent with the best-fit models used to describe the rest-frame UV to near-IR SED, which is all the more

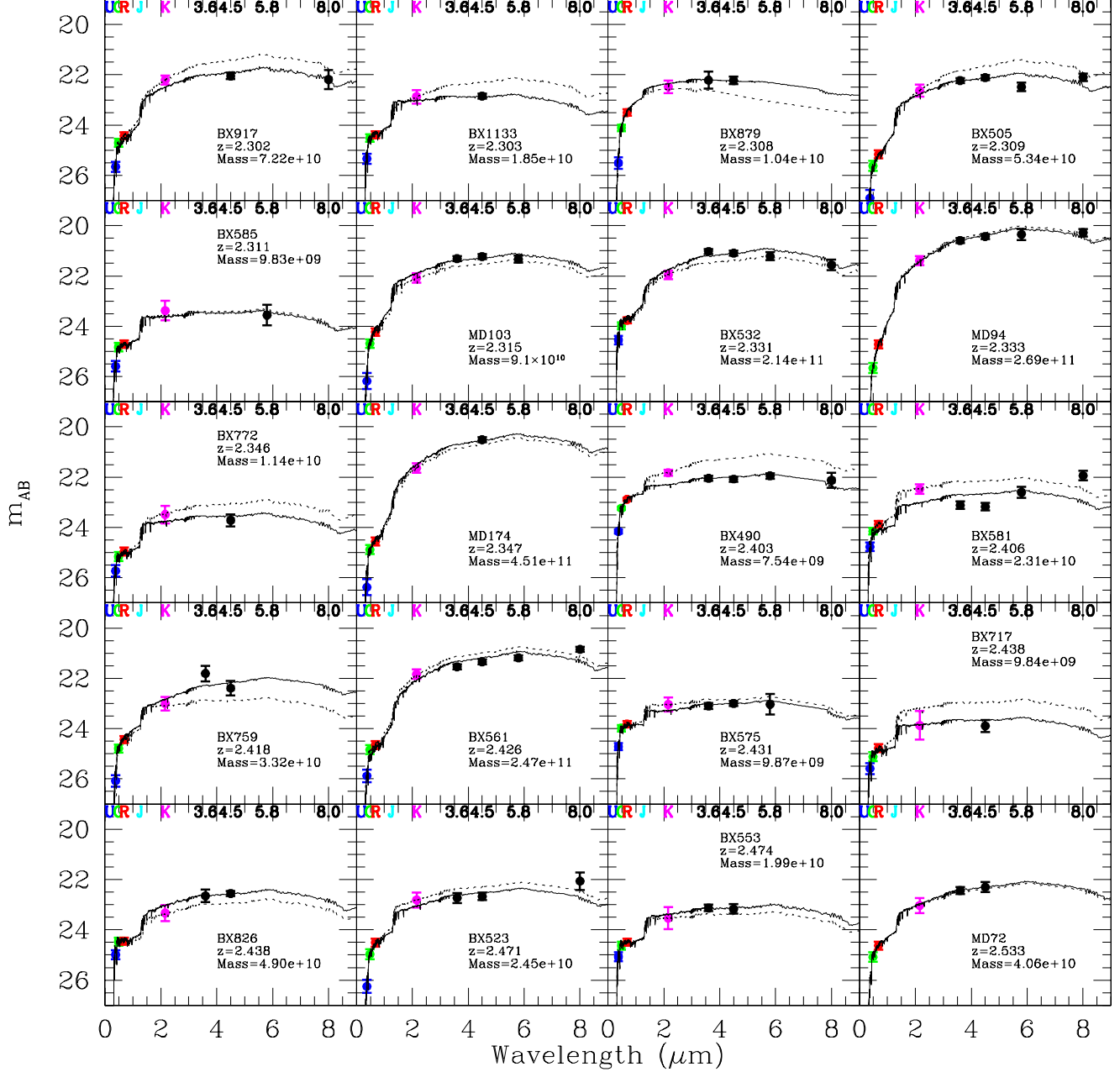


FIG. 5.— (continued)

striking since the models appear fairly well-constrained.

Clearly, there are cases in which the simple, single-component SED-fitting procedure fails to capture the true nature of the galaxy stellar population. Rest-frame UV and optical spectra, and X-ray, submillimeter, and radio fluxes, provide valuable complementary information that must be included to better-constrain all of the stellar population parameters. The limitations inherent in SED fitting, without external constraints (and especially without spectroscopic identifications), should be borne in mind when considering the resulting stellar population parameters. On the other hand, the stellar masses inferred for these three galaxies are largely independent of the star-formation history assumed, and

therefore we include them in all further discussion of stellar masses.

5. RESULTS

5.1. The Stellar populations of $z \sim 2$ Galaxies in the HS1700 Field

In Figure 5, we show the observed optical, near-IR, and *Spitzer* photometry and best-fit models for the entire sample of UV-selected $z \sim 2$ galaxies in the HS1700 field with spectroscopic redshifts, K_s , and *Spitzer*/IRAC photometry. The solid lines indicate best-fit exponential Bruzual & Charlot (2003) models including the IRAC measurements, whereas the dotted lines indicate fits to only U_nGRK_s photometry. The stellar mass inferred

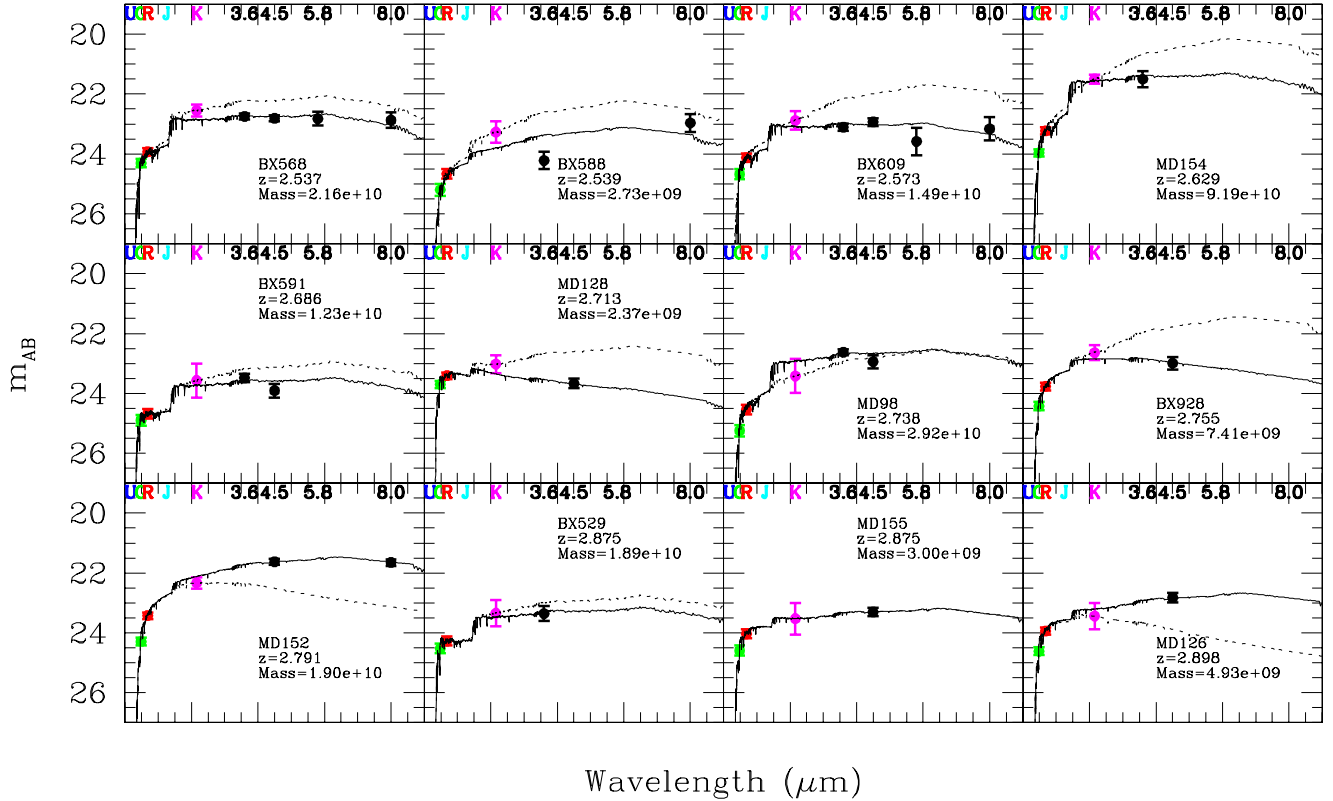


FIG. 5.— (continued)

from the best-fit to the entire SED (including IRAC photometry) is also shown, along with the redshift of each object. In Table 3, we list the best-fit stellar population parameters for each object, including the entire optical through IRAC SED. Parameters are listed for the best-fit model assuming $\tau = \infty$ (CSF), and also for the exponentially declining model that formally yielded the lowest value of χ^2 when τ was allowed to vary as a free parameter. There is a subset of galaxies with extremely young best-fit ages ($t_{sf} \leq 10$ Myr), for which all values of τ yield nearly identical stellar population parameters. These galaxies include: BX928, BX1075, BX794, MD128, BX879, BX490, MD152, BX588, and MD126. In such cases where t_{sf} is smaller than any of the τ values considered, the star-formation history (as parameterized by τ) becomes irrelevant.

From both Figure 5 and Table 3, it is clear that a large range of rest-frame UV to rest-frame near-IR SEDs is included in our sample. In particular, we highlight the variety of rest-frame UV/near-IR colors, which translates directly into a large range of inferred near-IR mass-to-light ratios.

5.2. Distribution of Stellar Masses

Figure 6 shows the distribution of stellar masses inferred from the optical-IRAC SEDs. The mass for each object is taken from column 7 of Table 3. The nearly log-normal distribution of stellar mass can be characterized by a mean and standard deviation $\log M_* = 10.32 \pm 0.51 M_{\odot}$. For the CSF models (the results of which are also compiled in table 3), we find a distribu-

tion $\log M_*(CSF) = 10.30 \pm 0.53$. Figure 7 compares the stellar mass obtained assuming the best-fit τ model to the stellar mass implied by the best-fit CSF models. The agreement, both in terms of the mass distribution and the masses of individual objects, is excellent, with no obvious systematic trend or offset.

For some purposes, it is of interest to break down the inferred stellar mass distribution as a function of observed K_s -band magnitude, since a number of other surveys of galaxies at similar redshifts are selected in that band. The results are summarized in Table 4, where the K_s limits are chosen to correspond to the limits imposed by some of these other surveys. As expected, there is a clear trend of increasing inferred stellar mass with increasing rest-frame optical luminosity, although, as discussed below, there is significant scatter in rest-optical M/L at a fixed mass or luminosity.

The typical (median) Monte Carlo uncertainties in individual stellar mass estimates are $\sim 30 - 35\%$, derived from simulations in which τ was allowed to vary as a free parameter. If we model all galaxies in the sample with CSF star-formation histories, we find that the median Monte Carlo stellar mass uncertainty is $\sim 35\%$. These values indicate that, for the same photometry and uncertainties, CSF models actually yield stellar mass uncertainties at least as large as the ones derived when τ is allowed to vary as a free parameter.

5.3. Results with and without Spitzer/IRAC Photometry

One of the fundamental limitations of the analysis in Shapley et al. (2001) and Papovich et al. (2001) was

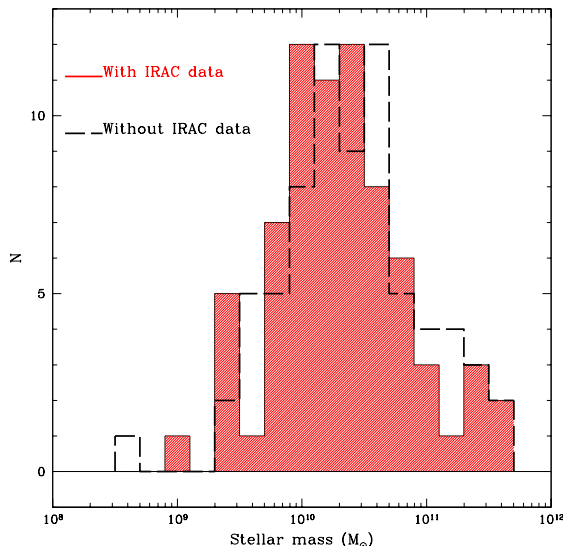


FIG. 6.— Histograms of best-fit stellar masses, with (shaded) and without (unshaded, dashed) IRAC photometry. As discussed in the text, the overall mass distribution and the total inferred stellar mass are similar to within $\sim 15\%$, although the uncertainties in the measurement of individual stellar masses are smaller by a factor of $\sim 1.5 - 2$ when the IRAC data are included.

the the inability to discriminate among different star-formation histories with only rest-frame UV and optical photometry. We have shown that, even with the addition of *Spitzer*/IRAC photometry, this inability to constrain star-formation histories persists for most galaxies in our $z \sim 2$ sample. The broad-band SEDs are particularly degenerate with respect to age, dust content, and star-formation rates, while the inferred stellar mass suffers from much less systematic uncertainty. Another question raised in the pre-*Spitzer* era was whether or not rest-frame near-IR photometry of $z \geq 2$ galaxies would uncover considerably more stellar mass from old bursts than had been inferred from SEDs whose longest wavelength measurement was the ground-based K_s band, corresponding to the rest-frame optical at the redshifts of interest here. Such stellar composite populations might have been revealed through IRAC fluxes in excess of the rest-frame near-IR extension of model fits to the rest-frame UV through optical SEDs.

Figure 8 shows the relationship between $M_*(\text{No IRAC})$, the stellar mass inferred when the IRAC photometry is excluded from the fit, and $M_*(\text{IRAC})$, the stellar mass derived using IRAC photometry. Figure 6 displays this relationship in one dimension, with the distribution of $M_*(\text{No IRAC})$ indicated as an unshaded histogram in front of the shaded histogram of $M_*(\text{IRAC})$. What both figures demonstrate is that, on average, the stellar mass inferred with and without IRAC data agree without a large systematic offset, though the scatter in this relationship is significant and larger than the typical (formal) uncertainties in the individual stellar mass estimates using the full SED. Table 4 compares these inferred stellar mass distributions as a function of limiting observed K_s flux.

The average of $\log M_*(\text{No IRAC}) - \log M_*(\text{IRAC}) = 0.06$, with a standard deviation of 0.35 dex; the median difference is only 0.01 dex. We find only five galax-

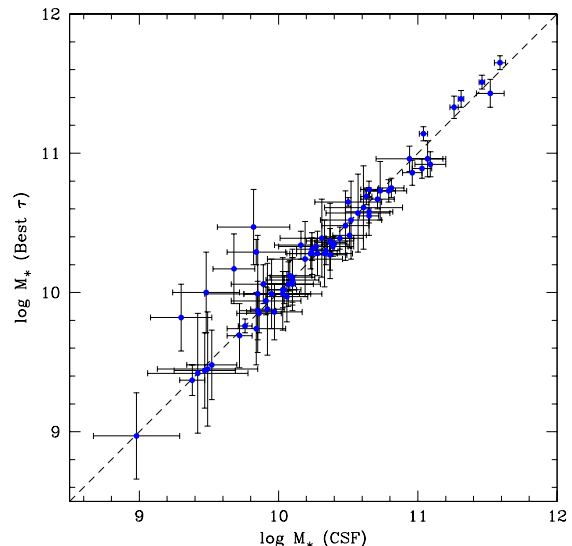


FIG. 7.— A comparison of the inferred stellar masses for constant star formation (CSF) models and for the best-fit declining star formation models (best τ) for the 72 galaxies with IRAC measurements. The error bars are as presented in Table 3, and are based on Monte Carlo modeling given the photometric errors. Note that there are no obvious systematic differences between the CSF and τ models, although in some cases the τ models result in significantly better agreement with the observed data.

ies whose optical-IRAC SEDs imply stellar masses more than a factor of two larger than that inferred from the optical- K_s SEDs. The most dramatic such example is BX898, whose observed $4.5\mu\text{m}$ flux is ~ 3.5 times larger than that predicted by the fit to the optical- K_s SED alone. The inferred stellar mass is ~ 12 times larger if the IRAC $4.5\mu\text{m}$ point is included in the SED fit. Unfortunately, BX898 has a significant IRAC measurement only at $4.5\mu\text{m}$, and contamination of this measurement (or, a statistical outlier in the observed K_s measurement) cannot be ruled out.

It is more common for the fit to the optical- K_s SED to *overpredict* the stellar mass relative to that inferred from the optical-IRAC SED. We believe that this discrepancy arises in most cases because of the contamination of the K_s continuum flux by $\text{H}\alpha + [\text{NII}]$ line emission at $2.0 \leq z \leq 2.5$. The addition of the IRAC photometry to the SEDs of galaxies with strong $\text{H}\alpha$ emission sometimes reveals the K_s data point as a positive outlier relative to the overall SED fit (e.g. BX794 and BX490), and the best-fit Balmer break is smaller than the observed $\mathcal{R} - K_s$ color alone would imply. In the absence of IRAC photometry, the K_s measurement strongly influences the inferred stellar mass because it is the only proxy for the strength of the Balmer break, resulting in a bias toward somewhat higher values. In support of this interpretation, for the four galaxies in the HS1700 K_s /IRAC pointings with published $\text{H}\alpha$ measurements, we find an average ratio of 1.55 between $M_*(\text{No IRAC})$ and $M_*(\text{IRAC})$ when no correction for $\text{H}\alpha$ emission is applied. When $\text{H}\alpha$ emission is corrected for, we find an average $M_*(\text{No IRAC})/M_*(\text{IRAC})$ of 1.11, i.e. closer to unity. More complete $\text{H}\alpha$ surveys are necessary to remove the K_s emission line bias, especially in order to model objects for which K_s is the reddest available band

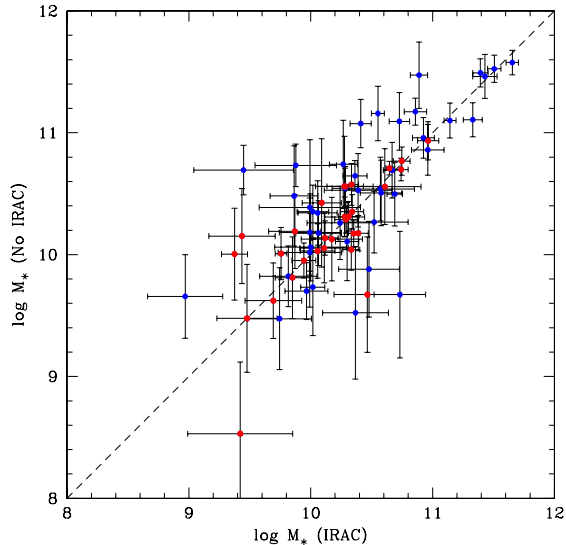


FIG. 8.— A comparison of the inferred stellar masses for the best-fit declining star formation models (best τ) for the 72 galaxies with IRAC measurements, derived with and without IRAC photometry. The error bars are based on Monte Carlo modeling given the photometric errors. There are very few galaxies for which the stellar mass is significantly underpredicted when IRAC photometry is excluded. It is more common for the no-IRAC fits to be biased towards higher stellar masses, in at least some cases because of the extra contribution to the K_s -band light by $H\alpha$ + [NII] emission. The red points are galaxies whose redshifts place $H\alpha$ outside of the K_s band, while the blue points are objects with $2.016 < z < 2.504$ for which significant contamination of the K_s measurement by $H\alpha$ emission is possible.

(Erb et al. 2005).

Without IRAC photometry, we find typical Monte Carlo stellar mass uncertainties of 50–60% for CSF models, which is ~ 1.5 times larger than the typical stellar mass uncertainties estimated when including the IRAC photometry. When τ is allowed to vary, the typical stellar mass uncertainty is 60–70%, ~ 2 times larger than the typical uncertainty inferred with IRAC photometry. Thus, while the lack of IRAC photometry does not appear to cause a large bias in the stellar mass estimates, the inclusion of IRAC photometry significantly reduces the formal uncertainties.

While we have noted the possibility of $H\alpha$ contamination of the K_s -band measurements for the $\sim 60\%$ of the current sample having redshifts where this is a potential problem, the *total* inferred stellar mass for the full sample of 72 galaxies differs by only $\sim 15\%$ when IRAC measurements are included or excluded (in the sense that the inferred total mass is higher without the IRAC data included). Thus, while the addition of longer-wavelength data leads to significantly smaller uncertainties in the estimates of the stellar masses of individual galaxies, the IRAC data do not appear to be essential for obtaining reasonable stellar mass estimates for galaxies at $z \sim 2$, particularly when statistics of large samples are most relevant.

5.4. Mass-to-Light Ratios versus Wavelength

It is often asserted that estimates of stellar mass from photometric measurements become increasingly reliable as one obtains longer wavelength data. We have certainly found this to be the case, as discussed above; however, it

is not true that long-wavelength observations can be used to measure stellar masses without understanding the recent star-formation history of the galaxy, even when observations extend into the rest-frame near-IR as for the IRAC observations of $z \sim 2$ galaxies. This point is illustrated in figures 9 and 10; we have chosen the observed K_s band and the observed IRAC channel 2 ($4.5\mu\text{m}$) band since the former is the longest wavelength measurement possible from the ground, and the latter lies close to $\sim 1.5\mu\text{m}$ in the rest frame at the mean redshift of the current sample (68/72 of the galaxies in the sample have been measured in IRAC channel 2), where the peak in the SED produced by older stellar populations is expected.

Figure 9 shows the absolute magnitude of the galaxies based on their observed K_s -band magnitudes, which at the median redshift of $\langle z \rangle = 2.29$ corresponds to rest-frame $0.65\mu\text{m}$ (i.e., R band). Note that while there is clearly a correlation between absolute R-band magnitude and stellar mass, there is a large enough range in star-formation history among the sample that a measurement of a particular rest-frame luminosity would map quite poorly onto stellar mass. The dotted and dashed curves show that there is a range in inferred M/L of a factor of ~ 70 among the sample. This large factor applies even for objects that are bright in the K_s band ($K_s \leq 20.0$), indicated with open circles. The very largest stellar M/L values approach that of present-day galaxies (Bell et al. 2003), but the average value is ~ 5 times smaller, $\langle (M/L)_R \rangle = 0.53$ (where both M and L are in solar units, and L is evaluated in the rest-frame R band). The situation is improved at $4.5\mu\text{m}$ (\sim rest-frame $1.4\mu\text{m}$), as shown in figure 10; the scatter in the stellar M/L is a factor of ~ 15 , with indications that the scatter decreases for the most luminous galaxies in the rest-frame near-IR, which tend to have M/L very close to that of present-day galaxies. The scatter in M/L is also greatly reduced when the sample is limited to objects with $R - K_s > 3.5$ (the reddest quartile), indicated with open squares. Still, among the total sample studied here, the average value is $(M/L)_{1.4\mu\text{m}} = 0.38$, roughly 2.5 times smaller than typical in the local universe at the same rest wavelengths. The local M/L ratios were derived with an IMF containing fewer low-mass stars than are found in the standard $0.1 - 100M_\odot$ Salpeter IMF, used for the current work. Adopting the “diet” Salpeter IMF used in Bell et al. (2003) would lower the average $z \sim 2$ M/L ratios by a factor of ~ 1.5 .

A simple interpretation of these results is that gauging the importance of current and recent star formation on the galaxy luminosities, even in the rest-frame near-IR, depends on the observations of the full UV-to-near-IR SED of the galaxy. That is, one cannot go directly from near-IR luminosity to stellar mass without knowledge of the likely contribution of young stars to that luminosity, which can only come from measurements at shorter wavelengths. The region of the spectrum that is most sensitive to the ratio between the current star formation and the integral of past star formation is between the UV and the visual, conveniently measured by the observed $R - K_s$ color in the current sample. This point is illustrated in figure 11, which shows that the inferred stellar mass is remarkably well-correlated with $R - K_s$. In fact, the correlation between $R - K_s$ color and inferred stellar mass is almost as significant as the correlation between stellar

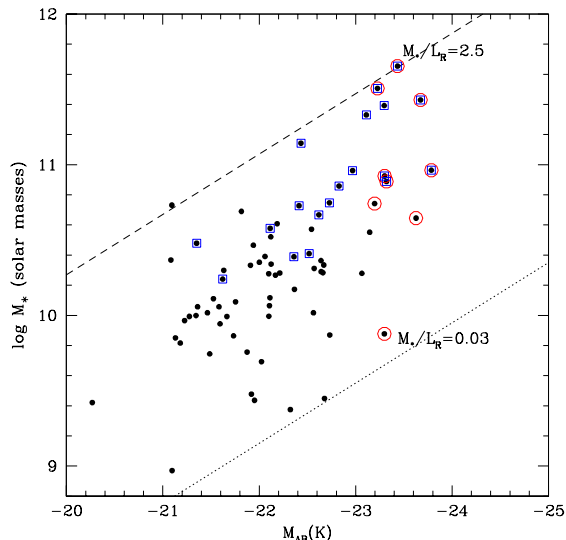


FIG. 9.— Inferred stellar mass for the best-fit model, versus the absolute magnitude at K_s ($2.155\mu\text{m}$). Note that the scatter in stellar mass/light ratios at a given K_s luminosity (rest-frame R band at the mean redshift of the sample) can be as large as a factor of 70. The 9 objects in the sample with $K_s \leq 20$ (Vega normalized) are indicated with open circles surrounding the points, while the reddest quartile of the sample with $\mathcal{R} - K_s > 3.5$ are indicated with open squares. Dashed and dotted lines bracket the range of stellar M/L in the sample, and are given in solar units, evaluated at rest-frame R band. The very largest optical stellar M/L seen in $z \sim 2$ galaxies approaches that of galaxies in the present-day universe, while the average value is ~ 5 times smaller.

mass and $M_{1.4\mu\text{m}}$ — using a Spearman test, the significance of the correlations are 5.9σ and 6.4σ , respectively — and more significant than the correlation between stellar mass and rest-frame $0.65\mu\text{m}$ absolute magnitude (5σ). One implication of this result is that, in the absence of IRAC data, it may be more effective to use $\mathcal{R} - K_s$ color rather than K_s flux to select $z \sim 2$ galaxies with large stellar masses. Another implication is that there are few galaxies that have large inferred stellar masses at $z \sim 2$ without showing evidence for long star-formation histories (cf., Shapley et al. 2004) that are suggested by red rest-frame $2000 - 6500 \text{ \AA}$ colors.

Of course, caution is required in assessing the true significance of correlations that are based on the model results and not on directly measured quantities; such is the case for all stellar mass estimates. To some extent the results in this section simply reflect how the observed SED is used to infer stellar mass by the modeling software, as a single smoothly declining or continuous episode of star formation that dominates the emission at all wavelengths from rest-frame UV through near-IR. In such a framework, the ratio of rest-frame UV to optical or near-IR light indicates the stellar M/L in a fairly robust manner (see section 4.3). We can obtain a different result for the stellar mass if we instead understand the galaxy UV-to-near-IR SED as the superposition of a young, roughly continuous episode of star formation and an old burst that peaked sometime in the past. In the most extreme case of a maximally-old burst and a very young ($t_{sf} \leq 10 \text{ Myr}$) continuous episode, the old burst will dominate the rest-frame near-IR light, the young episode will dominate the emission at rest-frame UV wavelengths, and the maximum possible stel-

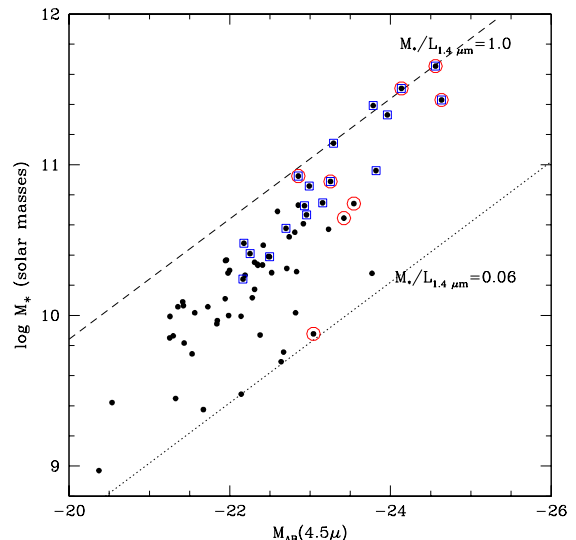


FIG. 10.— Inferred stellar mass for the best-fit model, versus the absolute magnitude at $4.5\mu\text{m}$, equivalent to the rest-frame $1.4\mu\text{m}$ luminosity at the mean redshift of the sample. As for figure 9, the objects with $K_s \leq 20.0$ are circled and those with $\mathcal{R} - K_s > 3.5$ are indicated with open squares. Dashed and dotted lines bracket the range of stellar M/L in the sample, and are given in solar units, evaluated at rest-frame $1.4\mu\text{m}$. While the scatter in stellar M/L is very much reduced compared to that measure in the K_s band, it can still be as large as a factor of 10 at a given $4.5\mu\text{m}$ luminosity. The $z \sim 2$ sample spans a range of a factor of 15, with the most massive galaxies having attained a near-IR M/L comparable to present-day galaxies, but with typical galaxies having $(M/L)_{1.4\mu\text{m}} \simeq 0.4$, a factor of ~ 2.5 smaller. There is much less scatter in near-IR M/L for objects with $\mathcal{R} - K_s > 3.5$.

lar mass will be inferred from the rest-frame near-IR luminosities. While this scenario is rather unrealistic, it does provide an extreme upper limit on the stellar mass implied by the rest-frame near-IR light. Less extreme multiple-component models provide a natural representation of the episodic star-formation histories that arise in a hierarchical model of galaxy formation, and will always result in *larger* stellar mass estimates than those derived from the single-component modeling presented thus far in this work.

In order to set a rough upper limit on the stellar masses implied by the broad-band SEDs, we used a technique very similar to that of Daddi et al. (2004b), which is designed to infer the maximum M/L ratio from the rest-frame near-IR data points. This method accounts for most of the light at those wavelengths with a maximally-old burst, on top of which is superimposed a young stellar population that accounts for most of the rest-frame UV emission. The ages of the maximally old models range from 2.2-4.3 Gyr for the galaxies in our sample. We first fit a young ($t_{sf} \leq 10 \text{ Myr}$) CSF model to the observed photometry, normalizing this model to the \mathcal{R} magnitude. We then subtracted this young model from the observed photometry, normalized the maximally old $\tau = 100 \text{ Myr}$ burst to the residual IRAC magnitudes, and summed the stellar mass from the two components. This sum is dominated by the mass of the old component, and is typically ~ 3 times larger than the single-component mass. The correlation between $M_{1.4\mu\text{m}}$ and stellar mass remains significant at the same level as for the single-component models. While $\mathcal{R} - K_s$ color is still significantly correlated

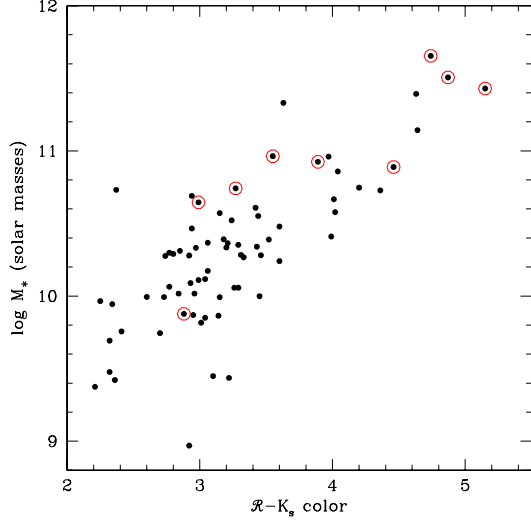


FIG. 11.— The relationship between inferred stellar mass and the observed $\mathcal{R} - K_s$ color for the sample of 72 galaxies with $\langle z \rangle = 2.26 \pm 0.30$. There is a very strong correlation between inferred M_* and $\mathcal{R} - K_s$ color, particularly for $\mathcal{R} - K_s > 3.5$. Again, objects with $K_s \leq 20.0$ are circled.

with stellar mass (at the $\sim 4\sigma$ level), the correlation is less significant than for the case of the single-component models discussed above. Specifically, there is much more scatter among objects with blue $\mathcal{R} - K_s$ colors, for which the M/L can change the most using this type of modeling. For objects with $\mathcal{R} - K_s > 3.5$, the inferred M/L and the correlation between stellar mass and $\mathcal{R} - K_s$ color are fairly insensitive to the type of model used.

It is easy to see that the amount of additional stellar mass that could be “hidden” by the current star formation episode is strongly dependent on the observed ratio of UV to optical/near-IR light. For the bluest objects, the ratio of true stellar mass to inferred stellar mass could be ≥ 5 while redder galaxies (except in extreme cases of dust obscuration) could not hide much additional stellar mass. For the galaxies in the sample with the largest stellar masses derived from single-component fits, the two component modeling provides stellar mass upper limits only 10–40% higher than the original estimates. Thus, in general, objects which already have large inferred stellar masses and old inferred ages cannot be much altered by more extreme assumptions, while objects that are completely dominated by the current episode of star formation (these would tend to be galaxies with very young inferred ages) could be more massive by factors as large as $\sim 5 - 10$. The typical BX/MD galaxy, which is between these extremes, probably has a true stellar mass that is a factor of ≤ 3 larger than the value inferred from population synthesis modeling. Finally, this decomposition of the SED into young and maximally-old components provides a fairly robust (but extreme) upper limit to the stellar mass consistent with the observed photometry, since more realistic, longer current star-formation episodes, would make an increasing contribution to the rest-frame near-IR light, and more realistic past bursts would occur at $z < \infty$ and have smaller M/L ratios.

5.5. AGN

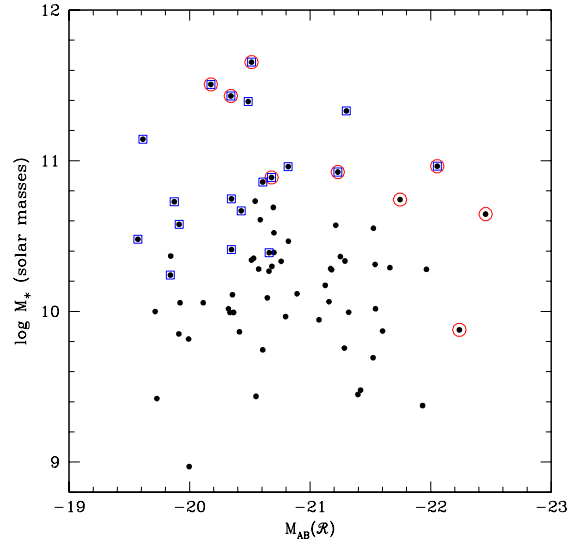


FIG. 12.— The relationship between the absolute magnitude in the observed \mathcal{R} band (equivalent to rest-frame 2100 Å at the mean redshift of the sample) and inferred stellar mass. A Spearman test indicates no correlation of these two quantities. There is a similar lack of correlation between M_* and the absolute magnitude at rest-frame ~ 1500 Å. Again, objects with $K_s \leq 20.0$ are circled and those with $\mathcal{R} - K_s > 3.5$ are indicated with open squares.

As described above, there is one object, MD157, whose spectrum shows clear signatures of AGN activity in the far-UV (strong C IV and He II emission as well as a broad Lyman α line). In addition, MD157 is extremely bright in the IRAC-4 band (AB mag of 18.51; see Table 2), such that obtaining a reasonable fit to its SED using stellar populations required excluding the $8\mu\text{m}$ data point. Two other objects, MD174 and MD94, have rest-frame optical spectra indicative of AGN (both have $\text{H}\alpha/[\text{NII}] \simeq 1$, and broad $\text{H}\alpha$ with $v_{\text{FWHM}} \geq 1000 \text{ km s}^{-1}$). All three objects exhibit significantly redder than average $\mathcal{R} - K_s$ colors, ranging from 4.46–5.15 and best-fit stellar masses ranging from $8 \times 10^{10} M_\odot$ to $4.5 \times 10^{11} M_\odot$.

An important question is how much the presence of the AGN affects the stellar mass estimates. The large stellar masses are inferred because of the bright rest-frame near-IR photometry and the very red rest-frame UV/optical and UV/near-IR colors, but if a dusty AGN were dominating the rest-IR part of the SED, these stellar mass inferences could be erroneous. A large fraction of other similarly bright and red $z \gtrsim 2$ galaxies having relevant spectroscopic measurements also indicate the presence of AGN. For example, 4 of the 7 galaxies with spectroscopic redshifts from the FIRES survey (Franx et al. 2003) presented by van Dokkum et al. (2003, 2004) exhibit UV and/or optical signatures of AGN activity (high ionization UV lines, broad $\text{H}\alpha$ and $\text{H}\alpha/[\text{NII}]$ line ratios near unity), similar to MD157, MD174, and MD94. It is difficult to know whether AGN activity leads to erroneously large stellar mass estimates, or whether it is preferentially objects that have already accumulated large stellar masses that tend to harbor significant AGN activity. When the AGN is not obviously energetically dominant in the observed-frame mid-IR, we suspect that the stellar mass estimates are probably reasonable; for objects like MD157, which is obvious as an AGN in both the rest-frame far-UV and near-IR, it is probably safest to assume

that the stellar mass has been over-estimated using SED fitting.

There are other objects that appear to have fluxes at $8\mu\text{m}$ that are significantly in excess of that expected from the SED modeling (e.g., BX756, BX535, MD69, BX505, BX581, BX561, BX523) but where we do not have any obvious spectroscopic evidence for the presence of an AGN. It is conceivable that these mid-IR excesses could be due to obscured AGN activity; deep Chandra images of this field could help resolve this question.

6. DISCUSSION

We have seen above that modeling of the broad-band SEDs of $z \sim 2$ star forming galaxies has significant limitations, even with spectroscopic redshifts and when longer-wavelength data are available for direct measurement of the rest-frame near-IR light. We have shown that reasonably consistent stellar mass estimates are obtained independent of the exact form of the star formation history, but that this consistency should be viewed with caution because of the fact that a robust episode of star formation can change the inferred M/L by a factor of several, even at rest-frame $\sim 1.5\mu\text{m}$. One obtains increasingly reliable estimates of the total stellar mass of a galaxy as the integral of star formation over the lifetime of the galaxy exceeds that in the past several hundred Myr by a factor of a few. In the most reliable cases, where the UV light is far surpassed by the emission at rest-frame optical and near-IR wavelengths, the inferred stellar mass does not depend very strongly on whether a smooth or episodic prescription is used to model the way in which the integrated stellar mass accumulated as a function of time. When the rest-frame UV luminosity is more comparable to rest-frame optical and near-IR luminosities, however, it is inevitable that the stellar masses inferred from photometric techniques will reflect the typical stellar mass produced in an episode of star formation, perhaps caused by a merger or accretion event over the course of the last few hundred Myr, and not the total stellar mass. A corollary to the above arguments is that it is most likely one would measure large stellar masses (using the type of modeling described in this paper) when the current rate of star formation is significantly smaller than the past average. Otherwise, most of the rest-frame near-IR and optical light will be ascribed to the current star-formation episode, which has much smaller M/L even in the IRAC bands. These are not new arguments (see, e.g., Papovich et al. 2001; Shapley et al. 2001), though the inclusion of IRAC wavelengths to constrain the rest-frame near-IR emission places them on a more robust footing, and the larger range of galaxy properties observed in the current sample highlights the important trends more clearly.

The concept of episodic star formation informs the above discussion. While such variable star-formation histories appear a reasonable representation of the build-up of stellar mass in galaxies at high redshift, simply based on general consideration of the hierarchical model of galaxy formation in which merging (and merger-induced star formation) plays a large role, we also find direct evidence from the galaxies in our sample. Specifically, we can obtain interesting constraints on the redshift at which the onset of star formation occurred for the galaxies in our sample, despite large systematic un-

certainities in the stellar population ages (section 4.3). The maximum stellar population age is obtained for a given set of rest-frame UV to near-IR colors when a continuous star-formation history is used, so we can use the CSF results to infer the earliest redshifts at which the current episodes of star formation could begin (cf., Ferguson et al. 2002). The median CSF age for the sample is ~ 600 Myr. Using the redshift and CSF age distributions we find that the current episode of star formation had not begun yet at $z = 3$ for at least $\sim 65\%$ (46/72) of the galaxies in the sample. The true fraction is probably higher, since CSF models provide only an upper limit on the age of the stellar population dominating the current star-formation episode. Therefore, we find that the majority of galaxies in our sample have young ages for the current episode of star formation compared to the age of the Universe at $z \sim 2$, allowing the possibility of much older previous bursts of star formation. Relatively young inferred ages would naturally arise in a picture of episodic star-formation.

A related point is that selecting on the basis of far-UV properties, as we have done for the BX/MD sample, connects only obliquely to stellar mass. One might expect that galaxies would have to attain a particular total mass threshold before they could support star formation detectable at the apparent magnitude limit of the survey, but once that threshold is exceeded, a combination of extinction (which is probably star-formation rate dependent; e.g., Adelberger & Steidel (2000)) and scatter in SFR per unit total (or stellar) mass might “randomize” the mix of galaxy properties included in the sample. Indeed, as shown in figure 12, we find that there is no hint of a correlation between M_{UV} and inferred stellar mass, as was found previously in the $z \sim 3$ LBG sample of Shapley et al. (2001).

These issues make it particularly difficult to measure the total stellar mass that has formed by a particular redshift (Dickinson et al. 2003; Glazebrook et al. 2004; Fontana et al. 2003), or to make a detailed comparison of the stellar mass of even similarly-selected galaxies at different redshifts. For example, analysis of the spatial clustering of $z \sim 3$ LBGs and $z \sim 2$ BX galaxies (Adelberger et al. 2004a) suggests that correlation length of LBG descendants at $z \sim 2$ would be similar to the observed BX correlation length, with the implication that $z \sim 2$ LBG descendants reside in dark matter halos in the same mass range as those hosting BX galaxies. It is therefore of interest also to compare the stellar mass distribution of spectroscopically-confirmed BX/MD objects with that of $z \sim 3$ LBGs from the sample of Shapley et al. (2001). A direct evolutionary comparison between the stellar mass distributions for $z \sim 2$ and $z \sim 3$ UV-selected samples is not straightforward for many reasons. Most importantly, while there is little doubt that the objects at $z \sim 2$ and $z \sim 3$ with large inferred masses and ages really are massive and old (see section 6.2), the modeling results likely represent lower limits on the stellar masses for more typical objects in both samples, where the current star formation is producing enough optical and near-IR light to potentially mask previous generations of stars. If star formation is episodic, as seems quite likely on many grounds, then it seems possible in principle that the same galaxy could be measured at different times, but the *inferred* stellar mass

might not even be a monotonically increasing function of time. Similarly, it might be difficult to trace the evolution of stellar mass during the epoch when most galaxies are still very actively star-forming.

Bearing all of these concerns in mind, we now summarize the inferred properties of typical UV-selected galaxies at $z \sim 2$. We then turn in some detail to the most massive and oldest galaxies in the sample, for which we obtain robust total stellar mass measurements, and show how these massive galaxies provide plausible progenitors for passive galaxies identified at $z \sim 1.5\text{--}2.0$. Finally, we make a general comment about the relationships among galaxy populations selected with different photometric criteria.

6.1. The Properties of the “Typical” UV-Selected Galaxy at $z \sim 2$

The results of this paper suggest that the typical $z \sim 2.2$ “BX” galaxy has a stellar mass of $\sim 3 \times 10^{10} M_\odot$, a number that could possibly be higher by a factor of $\sim 2\text{--}3$ without affecting the observed SEDs. Although the length of time stars have been forming in individual galaxies is not well-determined by the modeling, Steidel et al. (2005) show that galaxies within the significant over-density at $z = 2.30$ are older and contain more stellar mass on average than those in lower-density environments. It is very clear from these results that even at $z \sim 2$ the star-formation history is strongly dependent on large scale environment—more so than on the particular redshift at which the galaxies are observed. The typical current star-formation rate is $\sim 50 M_\odot \text{yr}^{-1}$ (Reddy & Steidel 2004), although unobscured star formation down to $\sim 3 M_\odot \text{yr}^{-1}$ could make it into the sample, and we know that among the BX sample lurk sub-mm sources that have implied SFR of up to $\gtrsim 1000 M_\odot \text{yr}^{-1}$ (Chapman et al. 2004). UV-selected galaxies that are also optically bright ($K_s \lesssim 20$) have typical inferred SFR higher by a factor of ~ 3 (Reddy et al. 2005a).

The space density of galaxies similar to those discussed in this paper is $\sim 3 \times 10^{-3} \text{ Mpc}^{-3}$ at $z \simeq 2.2$ (Reddy et al. 2005b). The co-moving correlation length of the UV-selected galaxies at $z \sim 2$ is $r_0 = 4.2 \pm 0.4 \text{ h}^{-1} \text{ Mpc}$ (Adelberger et al. 2005), implying that the typical galaxy lives in a dark matter halo of mass $\sim 2 \times 10^{12} M_\odot$. Assuming that the galaxies have a baryon fraction that is the same as the universal value, the estimated mass in baryons associated with the halo is $\sim 3 \times 10^{11} M_\odot$, suggesting that on average roughly 10% of the baryons have been converted into stars. Consideration of the expected evolution of the clustering properties of the UV-selected galaxies suggests that by $z \sim 1$ they will be found mainly among early-type galaxies, and will have completed most of their star formation. The most massive examples will have completed their star formation even earlier, and exhibit significantly stronger clustering than the average UV-selected galaxies at $z \sim 2$ (Adelberger et al. 2005). As discussed further in section 6.2 and other recent work, the ~ 2.5 Gyr between $z \sim 2$ and $z \sim 1$ marks the transition of a large fraction of massive galaxies from strongly star forming to largely quiescent (Daddi et al. 2004a; Shapley et al. 2004; Cimatti et al. 2004; McCarthy et al. 2004; Fontana et al. 2003).

6.2. Massive Galaxies in Rest-UV-Selected Samples

The most massive galaxies in the current sample, with stellar masses $> 10^{11} M_\odot$, cannot contain significant additional stellar mass that is masked by the current episode of star formation. We obtain roughly the same stellar mass estimate regardless of whether a single-component model is used to fit the colors, or a young current star-formation episode super-imposed on an old past burst. In the context of simple, single-component models, these galaxies also have SEDs that provide significant constraints on the star-formation history. Unlike the majority of galaxies in the HS1700 sample, for which we find that all or most τ values are consistent at the 95.4% level with the data, we can rule out models with $\tau < 200 \text{ Myr}$ and $\tau = \infty$ (i.e., CSF) for all but one of the galaxies with $M_* > 10^{11} M_\odot$. More discrimination among τ values leads to interesting constraints on the duration of the star-formation episodes in these galaxies. The minimum $\tau = 200 \text{ Myr}$ for these five galaxies implies minimum ages of $t_{sf} \geq 600\text{--}900 \text{ Myr}$. The most likely value of τ however is $1\text{--}2 \text{ Gyr}$, based on Monte Carlo simulations in which τ was allowed to vary. For $\tau = 1\text{--}2 \text{ Gyr}$, the ages inferred for these galaxies range from $2\text{--}3 \text{ Gyr}$, comparable to the age of the Universe at $z \sim 2.3$. The stellar masses for this subsample of galaxies are all well-constrained ($\leq 20\%$ uncertainties), including the systematic uncertainty in star-formation history⁸.

The superior constraint on star-formation history for these objects results from two factors: first, the most massive galaxies are among the brightest in the K_s and IRAC bands⁹, resulting in smaller than average $\mathcal{R} - K_s$ and IRAC photometric uncertainties. Four of the five massive galaxies with significant constraints on τ are also detected in all four IRAC bands, providing better constraints on the shape of the SED in the region dominated by longer-lived stars. Secondly, all but one of the objects with $M_* > 10^{11} M_\odot$ have significantly redder than average $\mathcal{R} - K_s$ (and $\mathcal{R} - \text{IRAC}$) colors¹⁰, but average or bluer than average $G - \mathcal{R}$ colors. The combination of blue to average $G - \mathcal{R}$ and red $\mathcal{R} - K_s$ colors indicates that the rest-frame optical and near-IR light cannot be ascribed to the massive stars tracing the instantaneous star-formation rate and dominating the rest-frame UV emission, and therefore must be produced by less massive stars formed primarily in the past. Since the inferred extinction correction will be small when the UV color is blue, either the star formation was much higher in the past, or the current SFR has been sustained for a very long time. If the implied CSF time is older than the age of the universe, then τ models will be required to fit the data well.

There are other objects in the sample with comparably small $\mathcal{R} - K_s$ and IRAC uncertainties, but with weaker

⁸ We note that the massive galaxies in the current sample are quite similar to those presented by Shapley et al. (2004), which were all drawn from another of our survey fields, Q1623+26.

⁹ We note, for comparison with the K20 survey (Cimatti et al. 2002) that only half of the galaxies in our sample with $M_* > 10^{11} M_\odot$ also have $K_s \leq 20.0$. A deeper apparent magnitude limit than $K_s = 20.0$ is evidently necessary to gain a complete census of the most massive galaxies at $z \sim 2$ (Glazebrook et al. 2004).

¹⁰ Most of the galaxies with $M_* > 10^{11} M_\odot$ have best-fit models with $J - K_s > 2.3$, implying that they would be selected by the FIRES survey.

constraints on τ . An example is MD94, which has very red $\mathcal{R} - K_s$ and $G - \mathcal{R}$ colors and is inferred to have a stellar mass $M > 10^{11} M_\odot$. In this case, the colors can be adequately fit by models spanning the whole range of τ , including CSF, mainly because the inferred current SFR (derived from the extremely red $G - \mathcal{R}$ color) is high enough to have produced the near-IR light in much less than the age of the universe, even for CSF. The best-fit τ model, though, has an age that is a factor of ~ 3 shorter than the CSF model, and a current SFR 3 times smaller (however, the implied initial SFR given the age and τ values would have been 25 times larger, or $2500 M_\odot \text{ yr}^{-1}$!).

We return now to the massive galaxies with superior constraints on the single-component star-formation histories. Of course, a smoothly-declining star-formation history is not a very likely scenario for the build-up of stellar mass, since the star-formation rate is expected to be modulated by episodic merger and accretion events. It is not really possible to establish whether or not star formation has been sustained continuously at a detectable level over a long period of time, even for galaxies whose star formation must have begun at very high redshift. For example, in general, galaxies for which the τ models are required for a good fit to single-component models can also be adequately fit by assuming a single, early burst of star formation to produce the optical/near-IR light and a small amount of recent star formation (with an associated stellar mass of only $\sim 1 - 2\%$ of the early burst) that accounts for the rest-frame far-UV light. For such two-component models, there is again no unique solution, but reasonable fits to the data can be found for models where a large burst with $\tau = 100 \text{ Myr}$ occurred at $z > 4$ and the recent (smaller) burst is less than 100 Myr old¹¹. While we cannot distinguish between smooth or episodic star-formation histories, the estimates of total stellar mass derived from two-component models agree very well with those obtained from the simple single-component fits. For these massive and old galaxies, the inferred total stellar mass is therefore a robust quantity.

In an analysis of the stellar populations of UV-selected $2.0 \leq z \leq 3.5$ galaxies in the *Hubble Deep Field* (HDF-N) Papovich et al. (2001) found no comparably massive and old objects. The small ratio between the typical inferred star-formation timescale for these HDF LBGs and the time interval between $2.0 \leq z \leq 3.5$ was used to motivate a scenario of multiple, intermittent star-formation episodes with a duty cycle of $\leq 1 \text{ Gyr}$. As described in the beginning of section 6, most of the current sample can in fact be described in this manner. In retrospect, it is not surprising that the sample of Papovich et al. (2001) did not contain any $M_* > 10^{11} M_\odot$ galaxies in the 5.0 arcmin^2 HDF-N field, despite a similar optical magnitude limit in the HDF spectroscopic sub-sample. We found only 6 with spectroscopic redshifts in the entire 65 arcmin^2 WIRC field. Since the spectroscopic completeness of our sample is $\sim 22\%$, the approximate surface density of objects in the redshift interval $z \simeq 2.3 \pm 0.4$ is $\sim 0.5 \text{ arcmin}^{-2}$, so that one would expect < 2 such massive and old galaxies in an

area with the size of the HDF-N given spectroscopic incompleteness. In fact, Labbé et al. (2003) have pointed out the discrepancy in the number of galaxies with red near-IR colors in the HDF-N versus their FIRES field in the HDF-S, with the HDF-N having only 10-20% of the numbers in the HDF-S. Given that the galaxies with large stellar mass are strongly clustered (Daddi et al. (2004b), Adelberger et al. (2005)) the variance between small survey areas is expected to be large for such rare objects.

6.3. UV-Selected Progenitors of Massive and Passive Galaxies?

While massive and mature galaxies represent a small fraction by number of the BX/MD population (6/72 with $M \geq 10^{11} M_\odot$, 5 of which also have $t_{SF} \sim$ the age of the Universe), their estimated space density, $\sim 10^{-4} \text{ Mpc}^{-3}$, is similar to the space density of the massive star-forming galaxies from the K20 survey presented by Daddi et al. (2004b) at $1.7 \leq z \leq 2.3$, and also the massive galaxies with old and passive stellar populations presented by Cimatti et al. (2004) and McCarthy et al. (2004) at $1.3 \leq z \leq 2.0$. In both of the latter papers, the authors suggest that the progenitors of the old and passive galaxies are to be found among submillimeter- and near-IR-selected samples at $z > 2$. Here we show that the most massive and mature objects in the $2.0 \leq z \leq 2.6$ UV-selected sample could quite plausibly be the progenitors of massive and passive systems at $1.3 \leq z \leq 2.0$. To make this comparison, we adopt star formation histories that are consistent both with those used to fit the near-IR selected massive and passive galaxies by Cimatti et al. (2004) and McCarthy et al. (2004) and with the SEDs of all 5 of the BX/MD massive and old galaxies at $z \sim 2.3$. We then evolve these models forward in time to the mean redshifts of the Cimatti et al. (2004) and McCarthy et al. (2004) samples, compute the average K_s magnitudes, $R - K_s$ and $I - K_s$ colors, stellar masses, and star-formation rates, and compare them with the properties of the passive galaxies.

Cimatti et al. (2004) present four galaxies at $\langle z \rangle = 1.7$, with $\langle K_s \rangle = 18.7$, $\langle R - K_s \rangle = 6.3$, stellar masses ranging from $1 - 3 \times 10^{11} M_\odot$, and a space density of $\sim 10^{-4} \text{ Mpc}^{-3}$. When a declining model with $\tau = 0.3 \text{ Gyr}$ is used to fit the colors, the associated ages and formation redshifts are $\sim 2 \text{ Gyr}$, and $z \sim 4$, respectively. If we apply a $\tau = 0.3 \text{ Gyr}$ model to the massive BX/MD SEDs at $\langle z \rangle = 2.3$, and then evolve them forward to $z = 1.70$, they would have $\langle K_s \rangle = 19.4$, $\langle R - K_s \rangle = 6.2$, $\langle M_* \rangle = 2.2 \times 10^{11} M_\odot$, ages ranging from 1.9-2.3 Gyr, and SFRs of $\leq 1 M_\odot \text{ yr}^{-1}$, making them fainter than $\mathcal{R} = 25.0$. We find a similar level of agreement between the BX/MD models evolved to $z = 1.5$ and the parameters of the 5 objects in McCarthy et al. (2004) (their table 1) for which a $\tau = 0.5 \text{ Gyr}$ model was used to fit the spectra and colors. Thus, extrapolating star formation histories for the massive BX/MDs forward in time would make them plausibly consistent with the passive galaxies in the near-IR selected samples observed at somewhat lower redshift. Equivalently, if the BX/MD examples are interpreted as massive old bursts with a small amount of recent star formation superposed, by $z \sim 1.7$ they would have essentially the same characteristics as the passive galaxies provided that the current episode of star forma-

¹¹ We note that such models would imply SFRs that averaged $\sim 1500 M_\odot \text{ yr}^{-1}$ over the first 200 Myr of the galaxy's life, e.g. between $z = 5$ and $z = 4.4$.

tion (i.e., as observed at $z \sim 2.3$) lasts for less than the ~ 900 Myr between $z \sim 2.3$ and $z \sim 1.7$.

The specific values of the timescale over which star formation occurs, and the redshift at which star formation begins, are not well-determined because of the systematic uncertainties inherent in stellar population synthesis modeling. However, we have demonstrated that, for reasonable assumptions (or at least consistent with those used by other workers), the most massive and evolved galaxies in the UV-selected sample are likely to evolve into largely passive systems by $z \sim 1.7$, with masses, ages, inferred formation redshifts, colors, and space densities similar to those of the massive and old stellar populations presented in the K20 and GDDS surveys. While additional progenitors of the $1.3 \leq z \leq 2.0$ massive and passive systems may be found among submillimeter- and $J-K$ color-selected samples, the UV-selected sample at $z \sim 2.3$ must contain a significant fraction of the objects that will look like elliptical galaxies at $1.3 \leq z \leq 2.0$.

Adelberger et al. (2004a) have reached similar conclusions about the fate of rest-UV-selected galaxies, using independent lines of argument. On the basis of a comparison of the observed clustering properties and galaxy number density at $z \sim 2$ with dark matter halos in numerical simulations, Adelberger et al. argue that the BX galaxies are consistent with typical total halo masses of $\gtrsim 10^{12} M_\odot$ and that by $z \sim 1$ they will have a clustering strength similar to that of galaxies with early type spectra in the DEEP2 redshift survey results of Coil et al. (2004). In this context, the most massive BX galaxies at $z \sim 2$ would be among the more extreme (in terms of clustering properties) early type galaxies by $z \sim 1$. Adelberger et al. (2005) has also shown that optically bright ($K_s \leq 20.5$) rest-UV-selected galaxies at $z \sim 2$, of which the most massive galaxies in the present sample are a subset, are as strongly clustered as their rest-optically selected counterparts (cf., Daddi et al. 2003, 2004b).

6.4. Selection Biases and “Populations”

We consider it likely that real galaxies actually evolve in and out of high redshift galaxy samples selected in various ways. For example, the massive galaxies in the BX/MD sample could easily have been sub-mm galaxies at $z \sim 4$ (when some versions of their star-formation histories predict high enough SFRs for them to have been easily detectable at $850 \mu\text{m}$, although most would probably not have been μJy radio sources because their redshift is too high), and may have oscillated between being quiescent and being UV-selectable depending on whether or not there was a trace of relatively unobscured star formation superposed on the more mature stellar populations.

As discussed by Shapley et al. (2004) and Adelberger et al. (2004a, 2005), the most massive and optically brightest galaxies in the UV-selected samples appear to have similar masses, chemical abundances, star-formation rates, inferred ages, and clustering properties as galaxies selected in the near-IR by either apparent brightness or optical/IR color. This comparison shows that a UV-selected survey is capable of finding examples of galaxies that are very similar to those selected in other ways; it is not a demonstration that a UV-selected survey “finds” the vast majority of galaxies at $z \sim 2$. That rest-UV selection is incomplete

with respect to all galaxies present at similar redshifts has been shown clearly by the near-IR selected GDDS, K20, and FIRES surveys as discussed above, as well as by sub-mm selected surveys (e.g., Chapman et al. (2003)). The point is that it is relatively easy for objects to come and go from a UV-selected surveys on timescales much shorter than a Hubble time at the relevant redshifts, independent of their past (or future) star-formation histories. Most of the existing evidence, and some theoretical studies (e.g., Nagamine et al. (2004)), suggests that at $z \sim 2$, relatively massive galaxies ($M_* \gtrsim 10^{10} M_\odot$) are “UV-selectable” using criteria similar to those employed in the current sample $\gtrsim 50\%$ of the time.

While such samples would be significantly incomplete with respect to all galaxies at a given stellar mass, they may not be entirely missing any type of galaxy. The fraction that happens to have enough UV light to be selected has significant advantages: spectroscopy is easy in both the far-UV and optical (rest frame). These observations allow for more detailed astrophysical studies, and an evaluation of the dependence of galaxy properties on large-scale environment as in Steidel et al. (2005). The recent success of the spectroscopic follow-up of sub-mm-selected galaxies (Chapman et al. 2004) has benefited from exactly the same advantage: even UV light that is inconsequential compared to the bolometric luminosity allows spectroscopic measurements, leading to more detailed astrophysical insight.

7. SUMMARY

We have presented a detailed analysis of the broadband SEDs of a sample of 72 rest-UV selected, spectroscopically confirmed, star forming galaxies at $z = 2.3 \pm 0.3$ in a ~ 8.5 by 8.5 arcmin field centered on HS1700+643. This sample of galaxies is broadly representative of galaxies selected with well-calibrated photometric pre-selection using rest-UV colors: all of the spectroscopic data were obtained without consideration of the longer-wavelength properties. We used extensive ground-based photometry from 0.35 - $2.15 \mu\text{m}$ and deep *Spitzer*/IRAC data probing the rest-frame near-IR, together with information from optical and near-IR spectroscopy, to produce an unprecedented data set that allows the most robust statements to date concerning the physical state of galaxies at $z \sim 2$, in particular their stellar masses.

Our main conclusions include the following:

1. Using population synthesis to model the stellar populations, we find that the inferred stellar mass distribution of the sample is reasonably well-described by a log-normal distribution: $\langle \log \frac{M_*}{M_\odot} \rangle = 10.32 \pm 0.51$ and that the result is essentially unchanged if a constant star formation history is assumed instead of the best-fitting exponentially declining star-formation history. The typical uncertainty in stellar mass, including variations in the assumed form of the star-formation history, is $\sim 30 - 35\%$. Sub-samples of the galaxies with brighter observed K_s ($2.15 \mu\text{m}$) flux have larger inferred stellar mass; 8% of the sample has inferred stellar mass $> 10^{11} M_\odot$. We found that fitting SEDs to simultaneously determine photometric redshifts and stellar population parameters leads to large uncertainties in both, and tends to over-estimate the inferred stellar mass; thus we use only the sample

with spectroscopic identifications.

2. The use of the *Spitzer*/IRAC fluxes, which measure the rest-frame near-IR light from the galaxies and thus should yield the strongest available constraints on stellar mass, provides a marked improvement in the estimates of the stellar mass of individual galaxies, reducing the formal uncertainties by a factor of $1.5 - 2$ relative to estimates based on photometry that extends only to the ground-based K_s band. However, we find that the longer wavelength data do not change the results significantly: the total stellar mass inferred for the entire sample of 72 galaxies is changed by only 15% depending on whether the *Spitzer* data are used for the modeling or not. At the redshifts spanned by our sample, there is a tendency to over-estimate slightly the stellar mass when the K_s band is the longest wavelength observed, because of contamination in the K_s band from $H\alpha$ emission.

3. The lack of strong constraints on the form of the star-formation history remains a problem for most of the galaxies in the sample, even when using simple, single-component models. Ages, exponential time constants, and extinction/SFR are largely degenerate with respect to each other; however, as found in previous work, the inferred stellar masses remain largely unaffected. External constraints can be used to rule out parts of parameter space that are otherwise allowed by the SED fits.

4. While the inferred stellar mass is correlated with the flux at $2\ \mu\text{m}$, the inferred stellar mass-to-light ratios can vary by a factor of ~ 70 at a given K_s -band luminosity (rest-frame R at the mean redshift of the sample). Even at an observed wavelength of $4.5\ \mu\text{m}$ (rest-frame $1.4\ \mu\text{m}$) the inferred M/L varies by a factor of 15. At both wavelengths (rest-frame 0.65 and $1.4\ \mu\text{m}$), the highest inferred M/L are similar to those of local galaxies, but the average M/L is a factor of at least 5 and 2.5 smaller, respectively. Thus, at these redshifts, even rest near-IR luminosities are by themselves a relatively poor proxy for stellar mass; the entire SED, from the UV to the near-IR, is essential. In particular, the conversion from rest-frame near-IR luminosity to stellar mass is strongly correlated with the observed $R-K_s$ color (rest-frame $2000-6500\ \text{\AA}$) which in the context of the models considered is a crude measure of the ratio of past to current star formation.

5. Even with IRAC rest-frame near-IR information, there remains the possibility of significant systematic underestimates of the stellar mass using single-component SED-fitting techniques; the magnitude of this effect depends sensitively on the shape of the SED. For objects that are red in their UV/optical and UV/near-IR colors, the mass inferred from SED fitting is unlikely to underestimate the stellar mass by more than a few tens of percent, while the bluest objects in the sample could

have total stellar masses that are as much as a factor of $\sim 5 - 10$ larger than inferred (in the case of the most extreme assumed star-formation histories). A typical object in our sample could be “hiding” up to a factor of ~ 3 more stellar mass than inferred by the modeling. Thus, for star-forming galaxies at high redshift, reasonably precise estimates of stellar mass are possible only for objects that are nearly finished forming stars, or caught in a relatively quiescent state between episodes of star formation. All other estimates should probably be considered as lower limits, possibly reflecting the typical stellar mass formed during a star-formation episode rather than the integrated stellar mass.

6. We have shown that the most massive galaxies in the UV-selected sample, with $M_* > 10^{11}\ M_\odot$, could plausibly evolve by $z \sim 1.7$ into the high redshift “passive” galaxies recently identified from near-IR selected spectroscopic surveys. The most likely star-formation histories for these UV-selected examples indicate that they began forming stars at very early times and that their star-formation rates were considerably higher in the past, quite similar to what is found for the near-IR selected galaxies. Taken together with the similarities in space density, stellar mass, chemical abundances, and clustering properties, galaxies with similarly large stellar masses should probably be treated as a single “population” regardless of the method used to discover them. In most cases, the UV light which brings them into the sample represents a small fraction of the stellar mass assembly.

This work is based in part on observations made with the *Spitzer* Space Telescope, which is operated by the Jet Propulsion Laboratory, California Institute of Technology under NASA contract 1407. Support for this work was provided by NASA through contract 125790, issued by JPL/Caltech. We are indebted to the IRAC instrument team, particularly Giovanni Fazio and Peter Eisenhardt, for obtaining and reducing the *Spitzer*/IRAC data in the HS1700+64 field, and for allowing us early access to the data. Kevin Bundy kindly provided excellent software for the reduction of the WIRC data. Paul Francis, the referee, provided comments that improved the manuscript. CCS, DKE, and NAR have been supported by grant AST03-07263 from the US National Science Foundation and by the David and Lucile Packard Foundation. KLA acknowledges support from the Carnegie Institution of Washington, and AES from the Miller Foundation for Basic Research in Science. We wish to extend special thanks to those of Hawaiian ancestry on whose sacred mountain we are privileged to be guests. Without their generous hospitality, the spectroscopic observations presented herein would not have been possible.

REFERENCES

- Abraham, R. G., Glazebrook, K., McCarthy, P. J., Crampton, D., Murowinski, R., Jørgensen, I., Roth, K., Hook, I. M., Savaglio, S., Chen, H., Marzke, R. O., & Carlberg, R. G. 2004, *AJ*, 127, 2455
- Adelberger, K. L., Erb, D. K., Steidel, C. C., Reddy, N. A., Pettini, M., & Shapley, A. E. 2005, *ApJ*, submitted
- Adelberger, K. L. & Steidel, C. C. 2000, *ApJ*, 544, 218
- Adelberger, K. L., Steidel, C. C., Pettini, M., Shapley, A. E., Reddy, N. A., & Erb, D. K. 2004a, *ApJ*, accepted (astro-ph/0410165)
- Adelberger, K. L., Steidel, C. C., Shapley, A. E., Hunt, M. P., Erb, D. K., Reddy, N. A., & Pettini, M. 2004b, *ApJ*, 607, 226
- Baldry, I. K. & Glazebrook, K. 2003, *ApJ*, 593, 258
- Barmby, P., Huang, J.-S., Fazio, G. G., Surace, J. A., Arendt, R. G., Hora, J. L., Pahre, M. A., Adelberger, K. L., Eisenhardt, P., Erb, D. K., Pettini, M., Reach, W. T., Reddy, N. A., Shapley, A. E., Steidel, C. C., Stern, D., Wang, Z., & Willner, S. P. 2004, *ApJS*, 154, 97
- Bell, E. F., McIntosh, D. H., Katz, N., & Weinberg, M. D. 2003, *ApJS*, 149, 289
- Bruzual, G. & Charlot, S. 2003, *MNRAS*, 344, 1000
- Calzetti, D., Armus, L., Bohlin, R. C., Kinney, A. L., Koornneef, J., & Storchi-Bergmann, T. 2000, *ApJ*, 533, 682
- Chabrier, G. 2003, *PASP*, 115, 763

- Chapman, S. C., Blain, A. W., Ivison, R. J., & Smail, I. R. 2003, *Nature*, 422, 695
- Chapman, S. C., Blain, A. W., Smail, I. R., & Ivison, R. J. 2004, *apJ*, submitted
- Cimatti, A., Daddi, E., Renzini, A., Cassata, P., Vanzella, E., Pozzetti, L., Cristiani, S., Fontana, A., Rodighiero, G., Mignoli, M., & Zamorani, G. 2004, *Nature*, 430, 184
- Cimatti, A., Pozzetti, L., Mignoli, M., Daddi, E., Menci, N., Poli, F., Fontana, A., Renzini, A., Zamorani, G., Broadhurst, T., Cristiani, S., D'Odorico, S., Giallongo, E., & Gilmozzi, R. 2002, *A&A*, 391, L1
- Coil, A. L., Davis, M., Madgwick, D. S., Newman, J. A., Conselice, C. J., Cooper, M., Ellis, R. S., Faber, S. M., Finkbeiner, D. P., Guhathakurta, P., Kaiser, N., Koo, D. C., Phillips, A. C., Steidel, C. C., Weiner, B. J., Willmer, C. N. A., & Yan, R. 2004, *ApJ*, 609, 525
- Cole, S., Norberg, P., Baugh, C. M., Frenk, C. S., Bland-Hawthorn, J., Bridges, T., Cannon, R., Colless, M., Collins, C., Couch, W., Cross, N., Dalton, G., De Propriis, R., Driver, S. P., Efstathiou, G., Ellis, R. S., Glazebrook, K., Jackson, C., Lahav, O., Lewis, I., Lumsden, S., Maddox, S., Madgwick, D., Peacock, J. A., Peterson, B. A., Sutherland, W., & Taylor, K. 2001, *MNRAS*, 326, 255
- Daddi, E., Cimatti, A., Renzini, A., Fontana, A., Mignoli, M., Pozzetti, L., Tozzi, P., & Zamorani, G. 2004a, *apJ*, in press (astro-ph/0409041)
- Daddi, E., Cimatti, A., Renzini, A., Vernet, J., Conselice, C., Pozzetti, L., Mignoli, M., Tozzi, P., Broadhurst, T., di Serego Alighieri, S., Fontana, A., Nonino, M., Rosati, P., & Zamorani, G. 2004b, *ApJ*, 600, L127
- Daddi, E., Röttgering, H. J. A., Labbé, I., Rudnick, G., Franx, M., Moorwood, A. F. M., Rix, H. W., van der Werf, P. P., & van Dokkum, P. G. 2003, *ApJ*, 588, 50
- Dickinson, M., Papovich, C., Ferguson, H. C., & Budavári, T. 2003, *ApJ*, 587, 25
- Erb, D. K., Shapley, A. E., Steidel, C. C., Pettini, M., Adelberger, K. L., Hunt, M. P., Moorwood, A. F. M., & Cuby, J. 2003, *ApJ*, 591, 101
- Erb, D. K., Steidel, C. C., Shapley, A. E., Pettini, M., & Adelberger, K. L. 2004, *ApJ*, 612, 122
- Erb, D. K., Steidel, C. C., Shapley, A. E., Reddy, N. A., Adelberger, K. L., & Pettini, M. 2005, *ApJ*, in preparation
- Fazio, G. G., Hora, J. L., Allen, L. E., Ashby, M. L. N., Barmby, P., Deutsch, L. K., Huang, J.-S., Kleiner, S., Marengo, M., Megeath, S. T., Melnick, G. J., Pahre, M. A., Patten, B. M., Polizotti, J., Smith, H. A., Taylor, R. S., Wang, Z., Willner, S. P., Hoffmann, W. F., Pipher, J. L., Forrest, W. J., McMurty, C. W., McCreight, C. R., McKelvey, M. E., McMurray, R. E., Koch, D. G., Moseley, S. H., Arendt, R. G., Mentzell, J. E., Marx, C. T., Losch, P., Mayman, P., Eichhorn, W., Krebs, D., Jhabvala, M., Gezari, D. Y., Fixsen, D. J., Flores, J., Shakoorzadeh, K., Jungo, R., Hakun, C., Workman, L., Karpati, G., Kichak, R., Whitley, R., Mann, S., Tollestrup, E. V., Eisenhardt, P., Stern, D., Gorjian, V., Bhattacharya, B., Carey, S., Nelson, B. O., Glaccum, W. J., Lacy, M., Lowrance, P. J., Laine, S., Reach, W. T., Stauffer, J. A., Surace, J. A., Wilson, G., Wright, E. L., Hoffman, A., Domingo, G., & Cohen, M. 2004, *ApJS*, 154, 10
- Ferguson, H. C., Dickinson, M., & Papovich, C. 2002, *ApJ*, 569, L65
- Fernández-Soto, A., Lanzetta, K. M., & Yahil, A. 1999, *ApJ*, 513, 34
- Fontana, A., Donnarumma, I., Vanzella, E., Giallongo, E., Menci, N., Nonino, M., Saracco, P., Cristiani, S., D'Odorico, S., & Poli, F. 2003, *ApJ*, 594, L9
- Franx, M., Labbé, I., Rudnick, G., van Dokkum, P. G., Daddi, E., Förster Schreiber, N. M., Moorwood, A., Rix, H., Röttgering, H., van de Wel, A., van der Werf, P., & van Starkenburg, L. 2003, *ApJ*, 587, L79
- Glazebrook, K., Abraham, R. G., McCarthy, P. J., Savaglio, S., Chen, H., Crampton, D., Murowinski, R., Jørgensen, I., Roth, K., Hook, I., Marzke, R. O., & Carlberg, R. G. 2004, *Nature*, 430, 181
- Kauffmann, G., Heckman, T. M., White, S. D. M., Charlot, S., Tremonti, C., Brinchmann, J., Bruzual, G., Peng, E. W., Seibert, M., Bernardi, M., Blanton, M., Brinkmann, J., Castander, F., Csábai, I., Fukugita, M., Ivezić, Z., Munn, J. A., Nichol, R. C., Padmanabhan, N., Thakur, A. R., Weinberg, D. H., & York, D. 2003, *MNRAS*, 341, 33
- Kennicutt, R. C. 1998, *ARA&A*, 36, 189
- Labbé, I., Franx, M., Rudnick, G., Schreiber, N. M. F., Rix, H., Moorwood, A., van Dokkum, P. G., van der Werf, P., Röttgering, H., van Starkenburg, L., van de Wel, A., Kuijken, K., & Daddi, E. 2003, *AJ*, 125, 1107
- Madau, P. 1995, *ApJ*, 441, 18
- McCarthy, P. J., Cohen, J. G., Butcher, B., Cromer, J., Croner, E., Douglas, W. R., Goeden, R. M., Grewal, T., Lu, B., Petrie, H. L., Weng, T., Weber, B., Koch, D. G., & Rodgers, J. M. 1998, in *Proc. SPIE Vol. 3355*, p. 81-92, *Optical Astronomical Instrumentation*, Sandro D'Odorico; Ed., Vol. 3355, 81-92
- McCarthy, P. J., Le Borgne, D., Crampton, D., Chen, H., Abraham, R. G., Glazebrook, K., Savaglio, S., Carlberg, R. G., Marzke, R. O., Roth, K., Jørgensen, I., Hook, I., Murowinski, R., & Juneau, S. 2004, *ApJ*, 614, L9
- Nagamine, K., Cen, R., Hernquist, L., Ostriker, J. P., & Springel, V. 2004, *ApJ*, submitted (astro-ph/0406032)
- Papovich, C., Dickinson, M., & Ferguson, H. C. 2001, *ApJ*, 559, 620
- Persson, S. E., Murphy, D. C., Krzemiński, W., Roth, M., & Rieke, M. J. 1998, *AJ*, 116, 2475
- Reddy, N. A., Erb, D. K., Steidel, C. C., Adelberger, K. L., Shapley, A. E., & Pettini, M. 2005a, *ApJ*, submitted
- Reddy, N. A. & Steidel, C. C. 2004, *ApJ*, 603, L13
- Reddy, N. A., Steidel, C. C., Adelberger, K. L., Shapley, A. E., Erb, D. K., & Pettini, M. 2005b, *ApJ*, submitted
- Rudnick, G., Rix, H., Franx, M., Labbé, I., Blanton, M., Daddi, E., Förster Schreiber, N. M., Moorwood, A., Röttgering, H., Trujillo, I., van de Wel, A., van der Werf, P., van Dokkum, P. G., & van Starkenburg, L. 2003, *ApJ*, 599, 847
- Schmidt, M., Schneider, D. P., & Gunn, J. E. 1995, *AJ*, 110, 68
- Shapley, A. E., Erb, D. K., Pettini, M., Steidel, C. C., & Adelberger, K. L. 2004, *ApJ*, 612, 108
- Shapley, A. E., Steidel, C. C., Adelberger, K. L., Dickinson, M., Giallisco, M., & Pettini, M. 2001, *ApJ*, 562, 95
- Steidel, C. C., Adelberger, K. L., Shapley, A. E., Erb, D. K., Reddy, N. A., & Pettini, M. 2005, *ApJ*, submitted
- Steidel, C. C., Adelberger, K. L., Shapley, A. E., Pettini, M., Dickinson, M., & Giallisco, M. 2003, *ApJ*, 592, 728
- Steidel, C. C., Shapley, A. E., Pettini, M., Adelberger, K. L., Erb, D. K., Reddy, N. A., & Hunt, M. P. 2004, *ApJ*, 604, 534
- van Dokkum, P. G., Förster Schreiber, N. M., Franx, M., Daddi, E., Illingworth, G. D., Labbé, I., Moorwood, A., Rix, H., Röttgering, H., Rudnick, G., van der Wel, A., van der Werf, P., & van Starkenburg, L. 2003, *ApJ*, 587, L83
- van Dokkum, P. G., Franx, M., Förster Schreiber, N. M., Illingworth, G. D., Daddi, E., Knudsen, K. K., Labbé, I., Moorwood, A., Rix, H., Röttgering, H., Rudnick, G., Trujillo, I., van der Werf, P., van der Wel, A., van Starkenburg, L., & Wuyts, S. 2004, *ApJ*, 611, 703
- Wilson, J. C., Eikenberry, S. S., Henderson, C. P., Hayward, T. L., Carson, J. C., Pirger, B., Barry, D. J., Brandl, B. R., Houck, J. R., Fitzgerald, G. J., & Stolberg, T. M. 2003, in *Instrument Design and Performance for Optical/Infrared Ground-based Telescopes*. Edited by Iye, Masanori; Moorwood, Alan F. M. *Proceedings of the SPIE*, Volume 4841, pp. 451-458 (2003), 451-458
- Yan, H., Dickinson, M., Eisenhardt, P. R. M., Ferguson, H. C., Grogin, N. A., Paolillo, M., Chary, R., Casertano, S., Stern, D., Reach, W. T., Moustakas, L. A., & Fall, S. M. 2004, *ApJ*, 616, 63

TABLE 1
HS1700+64 IMAGING OBSERVATIONS

Band	$\lambda_{\text{eff}}(\mu\text{m})$	Telescope ^a	Field Size	Integration	Seeing/Image Size	Photometric Depth ^b
U _n	0.36	WHT/Keck I 2001 May	15'3 × 15'3	23400/3600	0''89	26.4
G	0.47	WHT 2001 May	15'3 × 15'3	9900	0''83	26.5
\mathcal{R}	0.68	WHT 2001 May	15'3 × 15'3	7800	0''78	25.7
K _s	2.15	P200 2003 June/Oct	8'5 × 8'5	39720	0''84	24.0
IRAC-1	3.6	<i>Spitzer</i> 2003 Oct	5' × 10'	39600 ^c	2''02	24.6
IRAC-2	4.5	<i>Spitzer</i> 2003 Oct	5' × 10'	39600 ^c	2''38	24.3
IRAC-3	5.8	<i>Spitzer</i> 2003 Oct	5' × 10'	39600 ^c	2''36	23.0
IRAC-4	8.0	<i>Spitzer</i> 2003 Oct	5' × 10'	39600 ^c	2''56	22.8

^aWHT: William Herschel 4.2m telescope with Prime Focus Imager; Keck I: Low Resolution Imaging Spectrometer, blue side. P200: Palomar 5.1m telescope with Wide Field Infrared Camera; *Spitzer*: Spitzer Space Telescope/Infrared Array Camera

^bAB magnitude for a 5σ detection in a 2'' diameter aperture. For IRAC bands, the magnitude for a 5σ detection using PSF-fitting and local background estimation as described in the text

^cTotal exposure time in the deepest part of the mosaic. In general, the deepest regions of the IRAC-1 and IRAC-3 bands are in different parts of the field from those deepest in IRAC-2 and IRAC-4.

TABLE 2
HS1700+64 GALAXIES WITH SPECTROSCOPIC REDSHIFTS^a

Name	$\alpha(J2000)$	$\delta(J2000)$	z	\mathcal{R}_{AB}	$(G - \mathcal{R})_{AB}$	$(U_n - G)_{AB}$	$\mathcal{R} - K_s^b$	(IRAC-1) _{AB}	(IRAC-2) _{AB}	(IRAC-3) _{AB}	(IRAC-4) _{AB}
BX627	17:00:34.435	64:11:29.699	1.478	24.44±0.14	-0.10±0.05	0.12±0.05	2.36±0.51	...	23.63±0.18
BX738	17:01:16.150	64:12:36.684	1.710	23.93±0.12	0.01±0.04	0.49±0.09	3.29±0.15	22.11±0.10	22.15±0.10	22.56±0.29	23.07±0.49
BX756	17:00:55.146	64:12:54.403	1.738	23.21±0.11	0.33±0.05	0.58±0.09	2.41±0.23	...	21.82±0.10	...	21.55±0.15
BX681	17:01:33.762	64:12:04.278	1.740	22.04±0.05	0.19±0.01	0.40±0.02	2.99±0.08	21.02±0.10	21.08±0.10	21.16±0.18	21.35±0.14
BX843	17:01:15.627	64:13:52.891	1.771	24.61±0.16	0.18±0.08	0.51±0.11	3.26±0.31	22.95±0.34	22.80±0.10
BX470	17:01:26.563	64:09:31.993	1.841	24.26±0.14	0.38±0.07	0.75±0.13	4.20±0.11	21.44±0.10	21.45±0.10	21.30±0.10	21.69±0.13
BX846	17:01:02.925	64:13:54.470	1.843	23.91±0.12	0.09±0.04	0.48±0.09	3.18±0.18	...	22.13±0.10	...	22.15±0.33
BX574	17:00:46.904	64:10:49.536	1.846	24.10±0.14	0.24±0.07	0.73±0.10	3.43±0.19	22.31±0.10	22.27±0.10	22.06±0.22	22.99±0.36
BX1043	17:01:17.328	64:15:29.170	1.847	23.54±0.12	-0.01±0.05	0.53±0.09	2.34±0.42	...	22.78±0.24
BX1087	17:00:59.047	64:15:55.195	1.871	23.10±0.11	0.12±0.04	0.59±0.08	2.85±0.15	...	21.93±0.10
BX1032	17:00:52.827	64:15:23.792	1.883	23.76±0.12	0.18±0.04	0.62±0.06	3.04±0.18	...	22.37±0.10	...	22.59±0.30
BX782	17:01:11.146	64:13:14.360	1.930	23.94±0.12	0.05±0.04	0.59±0.09	2.97±0.22	22.18±0.15	22.35±0.11
BX530	17:00:36.859	64:10:17.376	1.942	23.05±0.11	0.21±0.05	0.69±0.05	2.80±0.15	21.73±0.10	21.88±0.10	...	22.19±0.33
BX807	17:00:54.909	64:13:28.593	1.971	24.83±0.16	0.08±0.08	0.45±0.11	3.04±0.36	...	23.49±0.10
BX903	17:00:54.431	64:14:14.761	1.976	24.39±0.14	0.18±0.06	0.50±0.11	2.99±0.28	...	22.80±0.10
BX536	17:01:08.939	64:10:24.949	1.977	23.00±0.11	0.21±0.05	0.79±0.05	3.27±0.10	21.23±0.10	21.20±0.10	21.23±0.10	21.83±0.12
BX412	17:01:20.109	64:08:37.363	1.981	23.58±0.12	0.31±0.06	0.63±0.06	3.31±0.15	22.13±0.10	22.23±0.10	22.32±0.14	...
BX526	17:00:58.040	64:10:15.947	2.018	23.99±0.12	0.00±0.04	0.45±0.09	2.25±0.42	22.90±0.24	22.94±0.23	23.05±0.34	...
BX1075	17:00:51.215	64:15:47.515	2.061	24.83±0.16	0.30±0.09	0.89±0.18	2.92±0.54	...	24.46±0.48
BX625	17:01:11.493	64:11:29.242	2.078	24.52±0.16	-0.03±0.07	0.49±0.06	2.96±0.54	23.28±0.10	23.28±0.10
BX592	17:01:02.703	64:11:03.422	2.099	24.87±0.16	0.38±0.09	1.11±0.19	3.01±0.36	23.35±0.11	23.43±0.12
BX535	17:01:07.597	64:10:26.403	2.113	25.16±0.16	0.57±0.12	1.55±0.37	3.45±0.37	23.04±0.14	22.89±0.17	22.82±0.22	22.78±0.33
BX1012	17:00:47.578	64:15:11.701	2.115	23.72±0.12	0.08±0.04	0.53±0.09	2.77±0.26	...	23.45±0.45
BX691	17:01:05.996	64:12:10.271	2.190	25.33±0.16	0.22±0.10	0.66±0.19	4.64±0.17	21.89±0.10	21.65±0.10	21.44±0.12	22.02±0.27
BX1118	17:01:08.914	64:16:12.554	2.214	24.55±0.16	0.07±0.08	0.57±0.11	3.14±0.36	...	23.67±0.29
BX1047	17:00:23.369	64:15:31.444	2.231	24.55±0.16	0.43±0.11	1.04±0.16	4.01±0.16	...	22.02±0.10	...	22.61±0.31
BX1084	17:01:32.349	64:15:50.699	2.245	23.76±0.12	0.45±0.07	1.05±0.11	3.89±0.10	...	22.14±0.46
BX931	17:00:25.497	64:14:29.805	2.246	25.15±0.16	0.47±0.12	1.12±0.28	3.60±0.28	...	22.83±0.11
BX794	17:00:47.301	64:13:18.702	2.253	23.60±0.12	0.35±0.06	0.58±0.09	3.10±0.18	...	23.67±0.25
BX1030	17:00:46.895	64:15:23.275	2.285	25.11±0.16	0.47±0.12	1.17±0.28	4.02±0.22	...	22.32±0.18
BX709	17:00:54.761	64:12:19.973	2.285	25.18±0.16	0.05±0.10	0.77±0.15	3.06±0.59	23.37±0.38	23.06±0.28
BX898	17:01:05.284	64:14:06.570	2.286	24.48±0.14	0.18±0.06	0.57±0.11	2.37±0.51	...	22.17±0.21
MD69	17:00:47.610	64:09:44.78	2.289	24.85±0.16	0.37±0.09	1.50±0.33	4.87±0.12	21.13±0.03	20.89±0.04	20.59±0.07	20.63±0.11
BX810	17:01:31.117	64:13:29.357	2.290	24.68±0.16	0.36±0.09	0.87±0.18	3.99±0.19	22.92±0.23	22.78±0.23
MD157	17:00:52.191	64:15:29.245	2.293	24.35±0.14	0.35±0.07	1.65±0.14	4.46±0.10	...	21.78±0.10	...	21.57±0.12
MD109	17:01:04.482	64:12:09.293	2.294	25.46±0.16	0.26±0.10	1.44±0.37	3.60±0.28	23.12±0.11	22.86±0.10
BX563	17:01:15.755	64:10:27.088	2.296	23.82±0.12	0.42±0.07	0.86±0.09	3.15±0.18	...	21.80±0.28
BX939	17:00:52.915	64:14:36.023	2.296	24.46±0.14	0.38±0.07	0.69±0.13	3.46±0.19	...	23.05±0.13
BX984	17:01:02.164	64:14:56.440	2.299	23.51±0.12	0.17±0.04	0.72±0.06	3.44±0.14	...	22.23±0.10
BX919	17:00:33.909	64:14:21.626	2.301	24.43±0.14	0.03±0.06	0.65±0.10	2.70±0.41	...	23.51±0.23
BX917	17:01:16.110	64:14:19.801	2.302	24.43±0.14	0.28±0.07	0.95±0.13	4.04±0.12	...	22.05±0.13	...	22.19±0.37
BX1133	17:01:03.294	64:16:19.717	2.303	24.38±0.14	0.14±0.06	0.82±0.13	3.33±0.23	...	22.85±0.10
BX879	17:01:17.768	64:13:55.116	2.308	23.50±0.12	0.61±0.04	1.40±0.19	2.84±0.22	22.22±0.34	22.22±0.15
BX505	17:00:48.224	64:10:05.862	2.309	25.17±0.16	0.45±0.12	1.28±0.26	4.36±0.19	22.23±0.10	22.11±0.10	22.49±0.17	22.10±0.15
BX585	17:01:13.491	64:10:58.829	2.311	24.71±0.16	0.12±0.08	0.76±0.13	3.15±0.36	23.56±0.41	...
MD103	17:01:00.209	64:11:55.576	2.315	24.23±0.14	0.46±0.09	1.49±0.27	3.97±0.12	21.32±0.10	21.23±0.10	21.34±0.14	...
BX532	17:00:40.154	64:10:22.537	2.331	23.76±0.12	0.22±0.06	0.57±0.09	3.63±0.12	21.02±0.10	21.10±0.10	21.21±0.16	21.56±0.21
MD94	17:00:42.020	64:11:24.224	2.333	24.72±0.16	0.94±0.15	2.06±0.25	5.15±0.15	20.59±0.08	20.43±0.03	20.35±0.22	20.28±0.14
BX772	17:00:53.076	64:13:04.566	2.346	24.96±0.16	0.20±0.09	0.57±0.14	3.29±0.31	...	23.72±0.25
MD174	17:00:54.542	64:16:24.760	2.347	24.56±0.16	0.32±0.09	1.50±0.27	4.74±0.11	...	20.51±0.10	...	18.51 ± 0.10
BX490	17:01:14.831	64:09:51.691	2.403	22.88±0.06	0.36±0.03	0.92±0.05	2.88±0.10	22.05±0.10	22.08±0.10	21.95±0.11	22.13±0.30
BX581	17:01:02.726	64:10:51.299	2.406	23.87±0.12	0.28±0.06	0.62±0.10	3.21±0.15	23.11±0.15	23.17±0.14	22.60±0.21	21.94±0.19
BX759	17:00:59.545	64:12:55.455	2.418	24.43±0.14	0.36±0.07	1.29±0.18	3.24±0.23	21.81±0.31	22.39±0.29
BX561	17:01:04.180	64:10:43.834	2.426	24.65±0.16	0.19±0.08	1.04±0.16	4.63±0.11	21.54±0.10	21.35±0.10	21.19±0.10	20.85±0.10
BX575	17:01:03.341	64:10:50.932	2.431	23.82±0.12	0.16±0.04	0.74±0.06	2.60±0.26	23.10±0.12	23.00±0.10	23.03±0.41	...

TABLE 2 — *Continued*

Name	$\alpha(J2000)$	$\delta(J2000)$	z	\mathcal{R}_{AB}	$(G - \mathcal{R})_{AB}$	$(U_n - G)_{AB}$	$\mathcal{R} - K_s^b$	$(IRAC-1)_{AB}$	$(IRAC-2)_{AB}$	$(IRAC-3)_{AB}$	$(IRAC-4)_{AB}$
BX717	17:00:56.995	64:12:23.763	2.438	24.78±0.16	0.34±0.09	0.47±0.13	2.73±0.54	...	23.89±0.24
BX826	17:01:17.163	64:13:41.960	2.438	24.45±0.14	0.02±0.06	0.52±0.09	2.94±0.28	22.65±0.25	22.55±0.10
BX523	17:00:41.712	64:10:14.884	2.471	24.51±0.16	0.46±0.11	1.28±0.18	3.52±0.25	22.74±0.20	22.68±0.15	...	22.07±0.35
BX553	17:01:02.200	64:10:39.390	2.474	24.49±0.14	0.14±0.06	0.44±0.11	2.77±0.41	23.13±0.13	23.18±0.19
MD72	17:00:42.777	64:10:05.346	2.533	24.63±0.16	0.45±0.11	1.51±0.00	3.42±0.25	22.44±0.15	22.30±0.20
BX568	17:01:28.789	64:10:46.682	2.537	23.93±0.12	0.38±0.06	0.94±0.09	3.20±0.15	22.75±0.10	22.81±0.10	22.82±0.23	22.87±0.25
BX588	17:01:01.469	64:11:00.301	2.539	24.67±0.16	0.53±0.11	1.17±0.19	3.22±0.31	24.22±0.29	22.97±0.29
BX609	17:01:9.988	64:11:15.663	2.573	24.12±0.14	0.56±0.09	1.33±0.18	3.06±0.27	23.10±0.12	22.94±0.13	23.58±0.46	23.16±0.38
MD154	17:01:38.387	64:14:57.372	2.629	23.23±0.11	0.73±0.04	1.91±0.22	3.55±0.09	21.50±0.27
BX591	17:00:50.179	64:11:01.162	2.686	24.68±0.16	0.22±0.09	1.06±0.16	2.93±0.54	23.48±0.14	23.91±0.23
MD128	17:00:30.292	64:13:15.165	2.713	23.41±0.11	0.29±0.04	1.24±0.08	2.21±0.28	...	23.67±0.16
MD98	17:01:04.387	64:11:49.543	2.738	24.54±0.16	0.70±0.10	1.82±0.46	2.94±0.54	22.62±0.10	22.94±0.22
BX928	17:01:19.623	64:14:25.911	2.755	23.77±0.12	0.66±0.07	1.54±0.19	2.95±0.22	...	22.99±0.21
MD152	17:00:31.085	64:14:54.048	2.791	23.43±0.11	0.86±0.05	1.92±0.29	2.92±0.15	...	21.62±0.10	...	21.65±0.11
BX529	17:00:44.618	64:10:19.001	2.875	24.27±0.14	0.25±0.06	0.28±0.06	2.74±0.41	23.35±0.25
MD155	17:00:47.888	64:15:05.446	2.875	24.03±0.14	0.56±0.09	1.83±0.43	2.32±0.51	...	23.31±0.14
MD126	17:00:51.610	64:13:05.346	2.898	23.94±0.12	0.67±0.04	2.01±0.46	2.32±0.42	...	22.82±0.15

^a Includes all galaxies with spectroscopic redshifts that are significantly detected in the ground-based K_s -band image and in one or more of the IRAC bands.

^b $\mathcal{R}(AB) - K_s(\text{Vega})$, to make the comparison with other samples easier. This color can be converted to the AB system used in the fitting and in the plots in Figure 5 by subtracting 1.82.

TABLE 3
MODELING RESULTS

Object	z	$\log M_*(\text{CSF})^a$	E(B-V)	SFR ^b	Age ^c	$\log M_*(\tau)^d$	E(B-V)	SFR ^e	Age ^f	τ^g
BX627	1.478	9.42±0.36	0.05	7	404	9.42±0.43	0.05	7	404	const
BX738	1.710	10.40±0.09	0.10	20	1278	10.35±0.05	0.00	4	404	100
BX756	1.738	9.76±0.05	0.34	377	15	9.76±0.05	0.34	377	15	const
BX681	1.740	10.50±0.24	0.21	246	128	10.65±0.03	0.08	1	81	10
BX843	1.771	9.89±0.23	0.21	24	321	10.06±0.14	0.04	1	255	50
BX470	1.841	10.81±0.09	0.30	64	1015	10.75±0.07	0.23	24	321	100
BX846	1.843	10.44±0.10	0.12	27	1015	10.39±0.08	0.03	7	360	100
BX574	1.846	10.16±0.19	0.24	51	286	10.34±0.10	0.06	3	255	50
BX1043	1.847	9.91±0.25	0.10	32	255	9.94±0.10	0.00	0	90	10
BX1087	1.871	10.24±0.11	0.15	68	255	10.31±0.08	0.04	3	114	20
BX1032	1.883	10.08±0.16	0.20	53	227	10.12±0.11	0.10	4	102	20
BX782	1.930	10.39±0.11	0.10	24	1015	10.33±0.07	0.00	6	360	100
BX530	1.942	9.84±0.21	0.34	699	10	10.29±0.09	0.08	1	72	10
BX807	1.971	9.86±0.16	0.10	10	719	9.85±0.14	0.01	3	321	100
BX903	1.976	10.10±0.16	0.14	22	571	10.11±0.20	0.10	13	360	200
BX536	1.977	10.65±0.06	0.23	138	321	10.74±0.06	0.09	20	203	50
BX412	1.981	10.24±0.18	0.20	61	286	10.28±0.15	0.12	16	161	50
BX526	2.018	10.06±0.15	0.04	16	719	9.97±0.18	0.00	8	255	100
BX1075	2.061	8.98±0.31	0.30	115	8	8.97±0.31	0.30	88	7	10
BX625	2.078	10.04±0.12	0.07	12	905	10.02±0.10	0.01	6	454	200
BX592	2.099	9.30±0.22	0.37	199	10	9.82±0.24	0.12	2	102	20
BX535	2.113	9.48±0.24	0.43	199	15	10.00±0.29	0.23	1	72	10
BX1012	2.115	10.10±0.20	0.07	25	509	10.06±0.19	0.01	10	255	100
BX691	2.190	11.04±0.03	0.29	40	2750	11.14±0.05	0.13	9	2750	1000
BX1118	2.214	9.97±0.20	0.07	13	719	9.86±0.20	0.00	4	286	100
BX1047	2.231	10.71±0.12	0.26	50	1015	10.67±0.07	0.12	8	404	100
BX1084	2.245	11.09±0.11	0.26	120	1015	10.92±0.09	0.10	15	404	100
BX931	2.246	10.19±0.27	0.27	38	404	10.24±0.27	0.20	15	255	100
BX794	2.253	9.49±0.36	0.29	430	7	9.45±0.41	0.28	265	7	10
BX1030	2.285	10.65±0.17	0.27	39	1139	10.58±0.17	0.23	22	454	200
BX709	2.285	10.37±0.17	0.10	10	2400	10.37±0.27	0.10	10	2400	const
BX898	2.286	10.73±0.11	0.10	20	2750	10.73±0.21	0.10	20	2750	const
MD69	2.289	11.46±0.02	0.35	105	2750	11.51±0.05	0.24	40	2200	1000
BX810	2.290	10.51±0.12	0.20	29	1139	10.41±0.09	0.01	3	454	100
MD157	2.293	11.03±0.07	0.28	66	1609	10.89±0.07	0.21	22	360	100
MD109	2.294	10.48±0.17	0.17	14	2100	10.48±0.25	0.17	14	2100	const
BX563	2.296	10.57±0.23	0.21	92	404	10.57±0.28	0.21	92	404	const
BX939	2.296	10.23±0.15	0.16	27	640	10.28±0.11	0.00	3	404	100
BX984	2.299	10.65±0.07	0.12	44	1015	10.55±0.05	0.01	10	360	100
BX919	2.301	9.84±0.21	0.07	17	404	9.74±0.26	0.00	5	161	50
BX917	2.302	10.96±0.07	0.18	33	2750	10.86±0.09	0.14	22	1015	500
BX1133	2.303	10.37±0.12	0.10	20	1139	10.27±0.11	0.01	5	360	100
BX879	2.308	10.03±0.10	0.42	1473	7	10.02±0.13	0.41	1380	7	100
BX505	2.309	10.79±0.13	0.28	38	1609	10.73±0.08	0.20	16	571	200
BX585	2.311	10.03±0.28	0.11	17	640	9.99±0.26	0.01	4	321	100
MD103	2.315	11.07±0.13	0.28	103	1139	10.96±0.13	0.21	38	321	100
BX532	2.331	11.26±0.03	0.14	65	2750	11.33±0.08	0.09	36	2750	2000
MD94	2.333	11.52±0.10	0.49	324	1015	11.43±0.10	0.42	113	321	100
BX772	2.346	10.07±0.18	0.10	12	1015	10.06±0.16	0.03	5	509	200
MD174	2.347	11.59±0.04	0.34	140	2750	11.65±0.05	0.20	40	2500	1000
BX490	2.403	9.92±0.12	0.29	835	10	9.88±0.33	0.28	506	9	10
BX581	2.406	10.37±0.11	0.11	33	719	10.36±0.10	0.10	26	509	500
BX759	2.418	10.52±0.22	0.23	73	454	10.52±0.28	0.23	73	454	const
BX561	2.426	11.31±0.02	0.29	79	2600	11.39±0.06	0.16	25	2400	1000
BX575	2.431	9.95±0.20	0.11	44	203	9.99±0.25	0.07	25	161	100

TABLE 3 — *Continued*

Object	z	log M _* (CSF) ^a	E(B-V)	SFR ^b	Age ^c	log M _* (τ) ^d	E(B-V)	SFR ^e	Age ^f	τ ^g
BX717	2.438	9.85±0.38	0.09	14	509	9.99±0.42	0.01	6	454	200
BX826	2.438	10.63±0.04	0.04	17	2600	10.69±0.06	0.01	11	2300	2000
BX523	2.471	10.31±0.30	0.25	71	286	10.39±0.28	0.18	28	227	100
BX553	2.474	10.34±0.10	0.04	14	1609	10.30±0.10	0.01	10	806	500
MD72	2.533	10.61±0.28	0.22	56	719	10.61±0.30	0.22	56	719	const
BX568	2.537	10.27±0.27	0.16	52	360	10.33±0.06	0.01	5	227	50
BX588	2.539	9.47±0.22	0.35	295	10	9.44±0.27	0.34	210	10	20
BX609	2.573	9.68±0.15	0.35	576	8	10.17±0.25	0.00	0	128	10
MD154	2.629	10.94±0.24	0.35	677	128	10.96±0.09	0.01	6	286	50
BX591	2.686	10.10±0.19	0.06	16	806	10.09±0.16	0.00	7	454	200
MD128	2.713	9.38±0.09	0.18	287	8	9.37±0.11	0.18	223	7	10
MD98	2.738	9.82±0.26	0.36	436	15	10.47±0.27	0.07	6	227	50
BX928	2.755	9.85±0.13	0.35	972	7	9.87±0.21	0.36	895	6	10
MD152	2.791	10.28±0.06	0.41	2087	9	10.28±0.16	0.41	2087	9	const
BX529	2.875	10.33±0.20	0.03	19	1139	10.28±0.24	0.01	15	640	500
MD155	2.875	9.52±0.18	0.26	333	10	9.48±0.25	0.24	202	9	10
MD126	2.898	9.72±0.09	0.29	520	10	9.69±0.23	0.28	380	10	20

^a Stellar mass and uncertainty, in solar units, for constant star formation model.^b Star formation rate, in M_⊙ yr⁻¹, for constant star formation model.^c Age, in Myr, for constant star formation model.^d Stellar mass and uncertainty, in solar units, for the best-fitting τ model. The stellar mass uncertainty reflects the uncertainty in τ .^e Star formation rate, in M_{sun} yr⁻¹, for the best-fitting τ model.^f Age, in Myr, for the best-fitting τ model.^g Best-fitting star-formation decay timescale (SFR $\propto e^{-\tau}$), in Myr.

TABLE 4
STELLAR MASS ESTIMATES AS A FUNCTION OF K_s MAGNITUDE

Sample	$\langle M_*(\tau) \rangle^a$	$\langle M_*(CSF) \rangle^b$	$\langle M_*(\tau) \rangle(\text{no IRAC})^c$
All (72)	10.32 ± 0.51	10.30 ± 0.53	10.37 ± 0.55
$K_s < 21$ (38)	10.56 ± 0.50	10.55 ± 0.51	10.67 ± 0.44
$K_s < 20.6$ (20)	10.75 ± 0.55	10.75 ± 0.56	10.88 ± 0.40
$K_s < 20$ (9)	10.96 ± 0.55	10.96 ± 0.55	11.01 ± 0.40

^a Mean and standard deviation of the log of the inferred stellar mass for the best-fit τ models.

^b Mean and standard deviation of the log of the inferred stellar mass for the CSF models.

^c Mean and standard deviation of the log of the inferred stellar mass for the best-fit τ model, excluding the IRAC photometry.

This figure "f1.jpg" is available in "jpg" format from:

<http://arxiv.org/ps/astro-ph/0503485v2>

This figure "f4.jpg" is available in "jpg" format from:

<http://arxiv.org/ps/astro-ph/0503485v2>